Hybrid Near-Far Field Channel Estimation for Holographic MIMO Communications

Shaohua Yue, *Graduate Student Member, IEEE*, Shuhao Zeng, *Member, IEEE*, Liang Liu, *Senior Member, IEEE*, Yonina C. Eldar, *Fellow, IEEE*, and Boya Di, *Member, IEEE*

***Abstract*— Holographic MIMO communications, enabled by large-scale antenna arrays with quasi-continuous apertures, are potential technology for spectrum efficiency improvement. However, the increased antenna aperture size extends the range of the Fresnel region, leading to a hybrid near-far field communication mode. The users and scatterers randomly lie in near-field and far-field zones, and thus, conventional far-field-only and near-field-only channel estimation methods may not work. To tackle this challenge, we demonstrate the existence of the *power diffusion* (PD) effect, which leads to a mismatch between the hybrid-field channel and existing channel estimation methods. Specifically, in far-field and near-field transform domains, the power of one channel path may diffuse to other positions, thus generating fake paths. This renders the conventional techniques unable to detect those real paths. We propose a PD-aware orthogonal matching pursuit (PD-OMP) algorithm to eliminate the influence of the PD effect by identifying the PD range, within which the path power diffuses to other positions. PD-OMP fits a general case without prior knowledge of respective numbers of near-field and far-field paths and the user's location. Simulation results show that PD-OMP can accurately estimate the channel when antenna spacing is below half wavelength and outperform current state-of-the-art hybrid-field channel estimation methods.**

***Index Terms*— Holographic MIMO communication, channel estimation, power diffusion, near-field communication.**

I. Introduction

TO FULFILL the high spectrum efficiency requirement of the future sixth-generation (6G) network [2], holographic MIMO communication has been proposed as a promising solution [3], [4], [5], where numerous antenna elements are integrated into a compact surface [6], [7], [8]. Potential implementation technologies include reconfigurable holographic surfaces [9], [10], extremely large reconfigurable intelligent surfaces [11], [12], [13], [14], and stacked intelligent surfaces [15]. Besides, far-field holographic MIMO channel estimation is studied in [16], where the rank deficiency of the spatial correlation matrix is exploited to optimize the least square (LS) estimator. Due to the increased radiation aperture size of the antenna array, the Fresnel region (radiating near-field region of the antenna) is significantly enlarged [17]. As a result, part of the users and scatterers lie in the near-field region of the holographic antenna array [18], where the EM waves are characterized by spherical waves [19], [20]. The remaining users and scatterers are located in the far-field region, and the EM waves can be modeled using uniform plane waves. This gives rise to the so-called *hybrid near-far field* communication [21], [22].

Channel estimation for hybrid-field communication can be mainly grouped into three categories: conventional methods such as LS and minimum mean square error (MMSE)-based methods [23], deep learning-based methods [24], and compressed sensing (CS)-based methods [21], [25], [26], [27]. Conventional methods require pilot signals to have at least the same dimension as the channel. Hence, a large pilot overhead is induced, especially for an extremely large antenna array. Deep learning-based estimation methods have been studied to reduce pilot overhead [24]. However, they may be limited in transferability since data collection and model training are required beforehand. In contrast, CS-based methods, such as greedy-based algorithms [21], [25], and graphic-based algorithms [27], which are transferable and demand pilot signals much fewer than LS or MMSE, serve as potential solutions to hybrid-field channel estimation.

Due to the modeling difference between near-field and far-field EM wave propagation, conventional CS channel estimation methods may not be directly applied to the hybrid-field case, necessitating the development of new schemes. Most existing works focus on either near-field channel estimation [28], [29], [30] or far-field channel estimation [31]. In [28] and [31], the polar domain and angular domain channel representation are proposed, respectively, to depict the characteristics of the near-field and far-field channel models. Some initial works [21], [25] consider the concept of a hybrid-field channel. Channel estimation techniques are designed relying on prior knowledge of the respective numbers of near-field and far-field paths such that the near-field and far-field path components are estimated separately [21], [25].

Manuscript received 2 January 2024; revised 13 May 2024; accepted 16 July 2024. Date of publication 1 August 2024; date of current version 13 November 2024. This work was supported in part by the National Key Research and Development Project of China under Grant 2022YFB2902800; in part by the National Science Foundation under Grant 62322101, Grant 62227809, and Grant 62271012; and in part by Beijing Natural Science Foundation under Grant 4222005 and Grant L212027. An earlier version of this paper was presented in part at the 2023 IEEE GLOBECOM [DOI: 10.1109/GLOBECOM54140.2023.10436807]. The associate editor coordinating the review of this article and approving it for publication was O. T. Demir. *(Corresponding author: Boya Di.)*

Shaohua Yue, Shuhao Zeng, and Boya Di are with the State Key Laboratory of Advanced Optical Communication Systems and Networks, School of Electronics, Peking University, Beijing 100871, China (e-mail: yueshaohua@pku.edu.cn; shuhao.zeng@pku.edu.cn; boya.di@pku.edu.cn).

Liang Liu is with the Department of Electronic and Information Engineering, The Hong Kong Polytechnic University, Hong Kong, SAR, China (e-mail: liang-eie.liu@polyu.edu.hk).

Yonina C. Eldar is with the Faculty of Mathematics and Computer Science, Weizmann Institute of Science, Rehovot 7610001, Israel (e-mail: yonina.eldar@weizmann.ac.il).

Color versions of one or more figures in this article are available at https://doi.org/10.1109/TWC.2024.3433491.

Digital Object Identifier 10.1109/TWC.2024.3433491

However, there exists a *power diffusion effect* in the sparse-signal-recovery-based hybrid-field channel estimation, which deteriorates estimation accuracy and has not been effectively addressed in the existing literature. Specifically, a high coherence may exist between some near-field and far-field steering vectors. Therefore, when a far-field (near-field) path is transformed from the spatial domain into the polar domain (angular domain), the power of this path component spreads to multiple steering vectors and generates fake paths. Such a high coherence also exists between some two near-field steering vectors, so the power can spread likewise when a near-field path is transformed from the spatial domain into the polar domain. Such an effect leads to an inaccurate path component estimation in the transform domain, which refers to the polar domain and the angular domain. This inaccuracy consequently causes estimation errors for the spatial-domain hybrid-field channel.

In this paper, we investigate hybrid near-far field channel estimation without any prior knowledge of the numbers of near-field and far-field paths. Against this background, two new challenges arise. *First*, it is non-trivial to distinguish the far-field and the near-field paths in the hybrid-field case. The boundary of the near-field and far-field regions is hard to specify since it changes with the propagation direction of the EM wave [32]. *Second*, due to the power diffusion effect, the power of near-field paths and far-field paths is coupled. It leads to inaccurate transform-domain path component estimation, which urges efficient channel estimation schemes.

To cope with the above challenges, we develop a power-diffusion-aware orthogonal matching pursuit algorithm (PD-OMP) for hybrid near-far field multipath channel estimation. The key idea of PD-OMP is two-fold. *First*, we observe that the angular domain can only provide accurate information about far-field path components, while the polar domain only provides precise information about near-field path components. Thus, we transform the spatial-domain hybrid-field channel to a joint angular-polar domain, where the near-field and far-field path components are successfully separated. *Second*, we define the *power diffusion range* to quantify the power diffusion from each path component to other positions. We demonstrate that the power diffusion range of each path is positively related to its power. Hence, by estimating the magnitude, direction, and propagation distance of each path component, the power diffusion range is calculated to identify and eliminate the interference brought by the power diffusion effect. In this way, the information on each path is extracted regardless of the power diffusion effect, and the hybrid-field channel is estimated accurately.

Our contributions are summarized below.

1) We analyze the power diffusion effect in the sparse-signal-recovery-based hybrid-field channel estimation, which leads to inaccurate transform-domain path component estimation. It reveals why conventional far-field and near-field sparse-signal-recovery-based channel estimation methods cannot be directly applied to the hybrid-field case. The power diffusion effect is also quantified by the *power diffusion range.*
2) We develop a power-diffusion-aware hybrid-field channel estimation method (PD-OMP), which does not require any prior information on the respective numbers of far-field and near-field paths to perform channel estimation. Employing an iterative CS-based method, PD-OMP introduces the power diffusion range to enhance the transform-domain path component estimation, which differs from other hybrid-field channel estimation techniques.
3) Simulation results show that the proposed PD-OMP achieves higher accuracy than state-of-the-art hybrid-field channel estimation techniques, given different SNRs and pilot lengths. The influence of scatterer distribution and the power diffusion range on algorithm performance are also discussed.

The rest of this paper is organized as follows. In section II, the holographic MIMO communication scenario, the hybrid-field channel model, and the signal model are described. In Section III, we present the hybrid-field channel characteristics in the joint angular-polar domain and analyze the power diffusion effect. A hybrid-field channel estimation method PD-OMP is proposed, and the Cramér-Rao Lower Bound of the sparse-signal-recovery-based hybrid-field channel estimation is derived in Section IV. In Section V, simulation results are provided, and conclusions are drawn in Section VI.

Throughout the paper, we use the following notation. Vectors and matrices are represented by lower-case and upper-case boldface letters, respectively. The writing $\mathbf{X} \in \mathbb{C}^{a\times b}$ means that the size of $\mathbf{X}$ is $a \times b$ and each element of $\mathbf{X}$ is a complex number. In addition, $\mathbf{X}(p,:)$ and $\mathbf{X}(:,p)$ denote the p-th row and p-th column of the matrix $\mathbf{X}$, respectively. We use $(\cdot)^T$, $(\cdot)^H$ and $(\cdot)^\dagger$ to denote the transpose, conjugate transpose, and pseudo-inverse operation, respectively. $|\cdot|$ is the absolute operator, $\mathrm{Tr}(\cdot)$ is the trace operator, and $\mathbb{B}(\mathbf{X}_1,\ldots,\mathbf{X}_N)$ represents a block diagonal matrix generated from matrices $\mathbf{X}_1,\ldots,\mathbf{X}_N$. $\mathrm{card}(\mathbb{A})$ denotes the number of elements in set $\mathbb{A}$.

II. System Model

In this section, we first describe the holographic MIMO communication scenario. The far-field and near-field path modeling are then given, respectively, based on which the hybrid-field channel model is presented. The signal model of pilot signal transmission is also provided.

A. Scenario Description

As shown in Fig. 1, we consider an uplink communication system. The base station (BS) is equipped with an extremely large linear antenna array[1] to communicate with a single-antenna user, with the number of antenna elements and the element spacing denoted by N and d, respectively. For a holographic MIMO system, it is assumed that $d \le \lambda/2$, where λ is the wavelength. We assume that the antenna elements are connected via $N_{RF} < N$ radio frequency (RF) chains such that the analog precoding scheme is employed at the BS. The EM radiation field of the antenna array can be divided into the near field and far field, as indicated in Fig. 1.

[1]The discussion on channel estimation in this paper is also applicable to the case of a planar array.

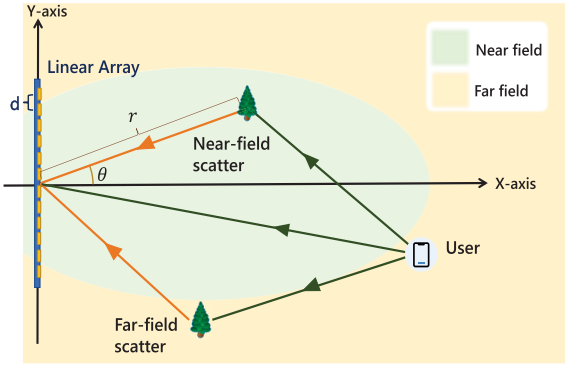

Fig. 1. Hybrid channel model with a linear holographic antenna array.

The boundary between these two fields depends on Rayleigh distance, which is positively correlated with the size of the antenna array [32]. Given the large size of the holographic antenna array, the near-field region extends, leading to *hybrid-field* communications, i.e., the user and scatterers can be located in either the near field or the far field of the antenna array.

B. Hybrid-Field Channel Model

Assume that the hybrid-field multipath channel from the user to the antenna array at the BS consists of a line-of-sight (LoS) path, denoted by path 0, and $L-1$ non-line-of-sight (NLoS) paths, denoted by paths $1, 2, \ldots, L-1$. In the following, we refer to the LoS path as far-field (or near-field) if the user lies in the far-field (or near-field) region of the antenna array, and we refer to an NLoS path as far-field (or near-field) if the scatterer corresponding to this path locates in the far-field (or near-field) region of the antenna array. For the hybrid-field channel, the L paths consist of both far-field and near-field paths. We first present the model for the far-field and near-field paths, respectively, which are then combined to obtain the hybrid-field channel. For simplicity, we introduce a Cartesian coordinate system, where the x-axis is perpendicular to the linear antenna array, and the y-axis is aligned with the antenna array. The location of the middle point of the antenna array is set to be $(0, 0)$, as depicted in Fig. 1.

1) Far-Field Path Modeling: For the user or the scatterer located in the far field of the antenna array, the EM wave of the far-field path received by the antenna array can be approximated by a uniform plane wave. In this case, if path l is a far-field path, where l is the index of path based on (6), the model for this path is described as [33]

$$\mathbf{h}_{F,l} = g_l \mathbf{a}(\theta_l), \tag{1}$$

where for the LoS path, i.e., $l = 0$, g_l represents the channel fading and θ_l is the angle between the x-axis and the direction from the origin to the user. For the NLoS path, i.e., $l \geq 1$, g_l is a random complex factor describing the joint impact of scattering and channel fading, and θ_l is the angle between the x-axis and the direction from the origin to the l-th scatterer. $\mathbf{a}(\theta_l)$ represents the far-field steering vector toward θ_l, i.e.,

$$\mathbf{a}(\theta_l) = \frac{1}{\sqrt{N}}[1, e^{jkd\sin(\theta_l)}, \ldots, e^{j\pi k(N-1)d\sin(\theta_l)}]^T, \tag{2}$$

where $k = \frac{2\pi}{\lambda}$ is the wavenumber of the EM signal.

2) Near-Field Path Modeling: When the user or the scatterer is located in the near field of the antenna array, we use a spherical wave model to describe the wavefront of EM waves, which is more accurate than the plane wave model. To capture this feature, if path l is a near-field path, the model for this path is described as [33]

$$\mathbf{h}_{N,l} = g_l \mathbf{b}(\theta_l, r_l), \tag{3}$$

where for the LoS path, i.e., $l = 0$, r_l is the distance between the origin and the user. For the NLoS path, i.e., $l \geq 1$, r_l is the distance between the origin and the l-th scatterer. The term $\mathbf{b}(\theta_l, r_l)$ is the near-field steering vector, expressed as

$$\mathbf{b}(\theta_l, r_l) = \frac{1}{\sqrt{N}}[e^{-jk(r_{1,l}-r_l)}, \ldots, e^{-jk(r_{N,l}-r_l)}]^T, \tag{4}$$

where $r_{n,l}$ is the distance between the n-th antenna element of the antenna array and the user or the l-th scatterer corresponding to this path. The term $r_{n,l}$ can be written as

$$r_{n,l} = \sqrt{(r_l\cos\theta_l)^2 + (t_n d - r_l \sin\theta_l)^2}, \tag{5}$$

where $t_n = \frac{2n-N+1}{2}$ and $(0, t_n d)$ is the coordinate of the n-th antenna element.

3) Overall Hybrid-Field Channel Modeling: Among the L paths, the set of the far-field and near-field paths from the user to the antenna array is denoted by $\mathbb{L}_F$ and $\mathbb{L}_N$, respectively, i.e., $L = \text{card}(\mathbb{L}_F) + \text{card}(\mathbb{L}_N)$. By combining near-field path components and far-field components, the hybrid-field multipath channel from the user to the BS is modeled as

$$\mathbf{h}_H = \sum_{l\in\mathbb{L}_F} \mathbf{h}_{F,l} + \sum_{l\in\mathbb{L}_N} \mathbf{h}_{N,l}. \tag{6}$$

C. Signal Model

During uplink channel estimation, the user continuously transmits pilot symbols to the BS for Q time slots. We assume that the channel coherent time is longer than the Q time slots so that channel state information (CSI) remains static during channel estimation. After the analog beamforming, the equivalent received pilot $\mathbf{y}_q \in \mathbb{C}^{N_{RF}}$ of the BS at time slot q is denoted as

$$\mathbf{y}_q = \mathbf{W}_q \mathbf{h}_H x + \mathbf{W}_q \mathbf{n}_q, \tag{7}$$

where x is the transmitted pilot signal and $\mathbf{W}_q \in \mathbb{C}^{N_{RF}\times N}$ is the beamforming matrix set at the BS. The term $\boldsymbol{n}_q \sim \mathcal{CN}(0, \sigma^2\mathbf{I}_{N\times N})$ is zero-mean complex Gaussian additive noise. The beamforming is configured with random phase shifts because no prior CSI is available in the channel estimation phase.

Based on (7), the received pilot signal at the BS over the entire Q time slots can be written as

$$\mathbf{y} = \mathbf{W}\mathbf{h}_H x + \mathbf{n}, \tag{8}$$

where $\mathbf{y} = [\mathbf{y}_1^T, \mathbf{y}_2^T, \ldots, \mathbf{y}_Q^T]^T \in \mathbb{C}^{N_{RF}Q\times 1}$, $\mathbf{W} = [\mathbf{W}_1^T, \mathbf{W}_2^T, \ldots, \mathbf{W}_Q^T]^T \in \mathbb{C}^{N_{RF}Q\times N}$, and $\mathbf{n} = [(\mathbf{W}_1\mathbf{n}_1)^T, (\mathbf{W}_2\mathbf{n}_2)^T, \ldots, (\mathbf{W}_Q\mathbf{n}_Q)^T]^T \in \mathbb{C}^{N_{RF}Q\times 1}$.

Due to a large number of antenna elements N, it may lead to a poor channel estimation accuracy if we view (8) as a system of linear equations and solve the real part and the imaginary part of each element in $\mathbf{h}_H$ directly from (8)

directly. This is because channel coefficients in $\mathbf{h}_H$ outnumber the pilot signals, i.e., $2N > QN_{RF}$. Alternatively, we can estimate the channel by distinguishing each path and estimating the $\{\text{real}(g_l), \text{imag}(g_l), \theta_l, r_l\}$ for each near-field path and $\{\text{real}(g_l), \text{imag}(g_l), \theta_l\}$ for each far-field path based on the received pilot signal $\mathbf{y}$. Therefore, the total number of parameters to be estimated is upper bounded by $4L$. Considering the limited number of multipath components at the millimeter wave frequency [21], we have $4L < QN_{RF}$. Therefore, a method to estimate the parameters of each path should be developed instead.

III. Characteristics of Hybrid-Field Channel

Because of the limited number of scatterers in the millimeter-wave communication [21], we aim to reduce the channel estimation overhead in (8) based on sparse signal recovery techniques. In existing works such as [28] and [31], sparse channel characteristics are revealed by transforming channels to the angular domain (or polar domain) for the far-field (or near-field) case. By exploiting the channel sparsity, sparse-signal-recovery-based channel estimation algorithms with low pilot overhead are designed [34].

However, in the hybrid-field case, if we apply the angular domain (or polar domain) channel transform, a power diffusion effect occurs. This effect indicates that the power of a path spreads to other positions and causes multiple fake paths to be detected. The non-orthogonality between the near-field and far-field steering vectors is the reason for such an effect. Thus, in the hybrid-field case, sparse channel representations can no longer be obtained via either the angular-domain transform or the polar-domain transform, which is shown explicitly below. Therefore, we apply a joint angular-polar domain channel transform, based on which the power diffusion effect is quantified by the power diffusion range. The power diffusion effect is then alleviated.

A. Introduction to Power Diffusion Effect

We first describe the angular-domain and the polar-domain channel transform, where the power diffusion effect of the hybrid-field channel is discovered. Next, the description of such an effect is given.

1) Angular-Domain Transform: The far-field channel $\mathbf{h}_F$ given in (1) is a weighted sum of steering vectors $\mathbf{a}(\theta)$ at different propagation directions of the EM waves, as given in (2). Therefore, a matrix $\mathbf{F}_A$ can be designed to transform a far-field channel $\mathbf{h}_F$ only consisting of far-field paths to the angular domain representation [35]:

$$\mathbf{h}_F = \mathbf{F}_A \mathbf{h}_{A,F}, \tag{9}$$

where $\mathbf{h}_{A,F} \in \mathbb{C}^{M\times 1}$ is the angular-domain representation of an arbitrary far-field channel $\mathbf{h}_F$. $\mathbf{F}_A = [\mathbf{a}(\theta_1), \mathbf{a}(\theta_2), \ldots, \mathbf{a}(\theta_M)] \in \mathbb{C}^{N\times M}$ and $\mathbf{a}(\theta_m)$, defined in (2), denotes that far-field steering vector toward direction θ_m. Two arbitrary steering vectors $\mathbf{a}(\theta_{m,1}), \mathbf{a}(\theta_{m,2})$ that constitute $\mathbf{F}_A$ should satisfy μ_Δ degree of orthogonality, which is denoted as,

$$|\mathbf{a}(\theta_{m,1})^H \mathbf{a}(\theta_{m,2})| \le \mu_\Delta, \tag{10}$$

where μ_Δ is the parameter to control the degree of orthogonality. Besides, θ_m are chosen such that $\sin(\theta_m)$ is evenly distributed among $(-1, 1)$ while satisfying (10), which is denoted as

$$\theta_m = \arcsin\left\{\frac{(2m-1-M)}{2M}\right\}, \ m = 1, \ldots, M, \tag{11}$$

Note that for an antenna array with antenna spacing d, the space dimension of far-field steering vectors $\{\mathbf{a}(\theta), \forall\theta\}$ is $\lfloor \frac{2dN}{\lambda} \rfloor$ [36]. Therefore, based on the CS theory [37], when $\mu_\Delta = 0$, $M = \lfloor \frac{2dN}{\lambda} \rfloor$ and $\mathbf{F}_A$ forms an orthonormal basis for the space of all $\mathbf{a}(\theta), \forall\theta$. When $\mu_\Delta > 0$, $M > \lfloor \frac{2dN}{\lambda} \rfloor$ forms an overcomplete dictionary. With an increased M, a refined angle sampling is provided so that path components with similar directions can be separated better. On the other hand, an increased d leads to an increase in the computational complexity.

2) Polar-Domain Transform: Similarly, a matrix $\mathbf{F}_P$ consisting of near-field steering vectors is designed to transform a near-field channel $\mathbf{h}_N$ only consisting of near-field paths to its representation in the polar domain, denoted as

$$\mathbf{h}_N = \mathbf{F}_P \mathbf{h}_{P,N}, \tag{12}$$

where $\mathbf{F}_P$ is obtained by sampling both angles and distances in the space and $\mathbf{h}_{P,N}$ is the polar-domain representation of an arbitrary near-field channel $\mathbf{h}_N$. Specifically,

$$\mathbf{F}_P = [\mathbf{F}_{P,1}, \mathbf{F}_{P,2} \ldots \mathbf{F}_{P,S}] \in \mathbb{C}^{N\times MS_P}, \tag{13}$$

$$\mathbf{F}_{P,s} = [\mathbf{b}(\theta_1, r_{s,1}), \mathbf{b}(\theta_2, r_{s,2}) \ldots \mathbf{b}(\theta_M, r_{s,M})], \quad s = 1, \ldots, S_P, \tag{14}$$

where the term $\mathbf{b}(\theta_m, r_{s,m})$, defined in (4), is the near-field steering vector toward position $\{\theta_m, r_{s,m}\}$ and S_P is the number of submatrices in the near-field polar domain. The main principle of the polar-domain codebook design is to minimize the coherence between near-field steering vectors. The angle θ_m is discretized in the same as the far-field angular domain in (11). The design of distance is given as

$$r_{s,m} = \frac{N^2 d^2 (1 - \sin^2(\theta_m))}{2s\lambda\beta_\Delta^2}, s = 1, \ldots, S_P, m = 1, \ldots, M, \tag{15}$$

where β_Δ is a parameter to limit the coherence between two steering vectors at the same direction θ_m. S_P is selected so that the boundary between the radiative near-field region and reactive near-field region is close to $r_{S_P,m}, \theta_m = 0°$.

Based on (15), it can be concluded that an increased number of submatrices S_P will increase the area sampled by the steering vectors because $r_{S,m}$ is inversely proportional to S and $(r_{S,m} - r_{1,m})$ increases as S increases for each m. Besides, parameter β_Δ controls both the density and size of the area sampled by $\mathbf{F}_P$. An increase in β_Δ provides a small sampling interval and a reduced area to be sampled.

3) Power Diffusion Effect: The *Power diffusion effect* refers to the phenomenon that when a path component is transformed from the spatial domain into the angular domain or the polar domain, the power corresponding to this path component spreads to other positions and generates fake paths, which are represented by multiple steering vectors.

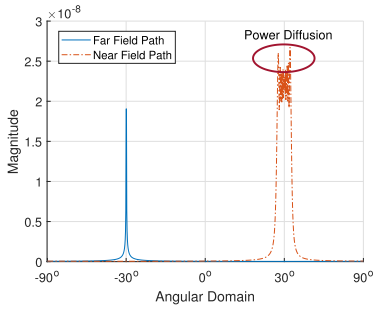

Fig. 2. The angular-domain transform result of a hybrid-field channel consisting of a far-field path and a near-field path.

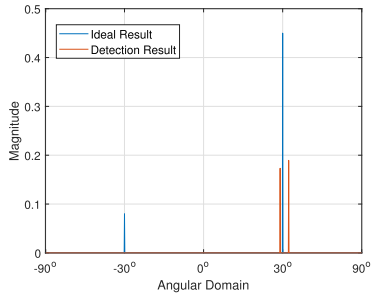

Fig. 4. The incorrect path detection result using 2-iteration OMP based on Fig. 2. The error comes from the power diffusion effect.

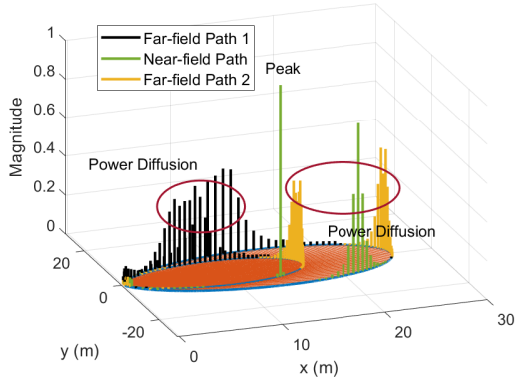

Fig. 3. The polar-domain transform result of a hybrid-field channel consisting of two far-field paths and a near-field path.

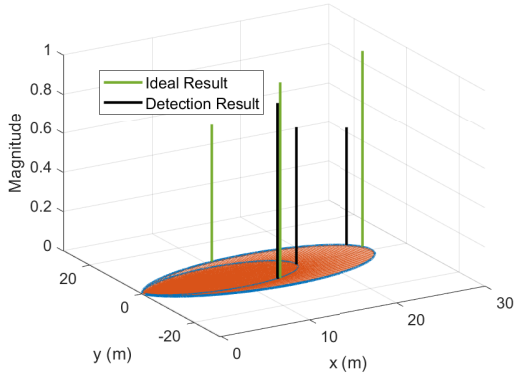

Fig. 5. The incorrect path detection result using 3-iteration OMP based on Fig. 3. The error comes from the power diffusion effect.

To demonstrate the power diffusion effect, in Fig. 2 we illustrate the angular-domain representation of a hybrid-field channel $\mathbf{h}_H$, which is defined in (6) and consists of a far-field path and a near-field path. The polar-domain representation of a hybrid-field channel consisting of two far-field paths and one near-field path is shown in Fig. 3. They are obtained by

$$\mathbf{h}_{A,H} = |\mathbf{F}_A^H \mathbf{h}_H|, \tag{16}$$

$$\mathbf{h}_{P,H} = |\mathbf{F}_P^H \mathbf{h}_H|. \tag{17}$$

As shown in Fig. 2, the power of the near-field path is not concentrated in one steering vector but spreads over multiple far-field steering vectors in the angular-domain transform matrix $\mathbf{F}_A$. Thus, multiple far-field steering vectors should be jointly applied to describe the near-field path. Similarly, in the polar domain, the far-field path should be described by multiple near-field steering vectors, as shown in Fig. 3. Also, it can be observed that the power diffusion effect exists for a near-field path to be transformed to a polar-domain transform matrix consisting of multiple submatrices, as depicted in Fig. 3.

The power diffusion effect is caused by the high coherence between two near-field steering vectors or the high coherence between near-field and far-field steering vectors in the transform domain. Formally, high coherence can be expressed as,

$$\mu_{p,q} = |\mathbf{b}(\theta_p, r_p)^H \mathbf{b}(\theta_q, r_q)| > \alpha, \tag{18}$$

$$\mu_{r,q} = |\mathbf{a}(\theta_r)^H \mathbf{b}(\theta_q, r_q)| > \alpha, \tag{19}$$

where α is a positive constant, $\mathbf{b}(\theta_p, r_p)$ and $\mathbf{b}(\theta_q, r_q)$ are two different near-field steering vectors as defined in (4), and $\mathbf{a}(\theta_r)$ and is a far-field steering vector as defined in (2). The terms $\mu_{p,q}, \mu_{r,q}$ denote the coherence between two steering vectors. To quantify the power diffusion effect, we define the *power diffusion range* as the range of steering vectors whose coherence with the steering vector representing the path is larger than a pre-defined threshold α.

Due to the power diffusion effect in the angular-domain and polar-domain channel representation, the issue of *inaccurate transform-domain path component estimation* arises, which consequently causes errors in spatial-domain channel estimation. We illustrate inaccurate transform-domain path component estimation based on conventional OMP channel estimation [37], as shown in Fig. 4 and Fig. 5. OMP aims to search for L peaks in the transform-domain channel representation, which represent the L path components of the multipath channel. The estimation result of transform-domain channel representation, consisting of the magnitude and corresponding steering vectors for the L peaks, provides sufficient information to restore the CSI.

However, the power diffusion effect causes multiple steering vectors within the power diffusion range, more than L in number, to carry channel information. For instance, in Fig. 2, the steering vectors that provide information for the near-field path are within the range of the ellipse. Since OMP only identifies L steering vectors, the steering vector representing the far-field path is omitted, resulting in an inaccurate estimation of the transform-domain path component, as shown in Fig. 4. Besides, it can be observed from Fig. 5 that the near-field path is correctly detected. However, due to the power diffusion effect of the far-field paths, two steering vectors in the power

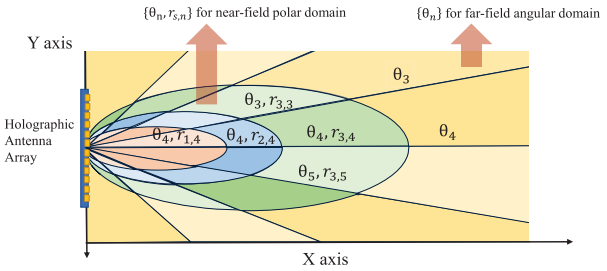

Fig. 6. The illustration of steering vectors in the joint angular-polar domain transform.

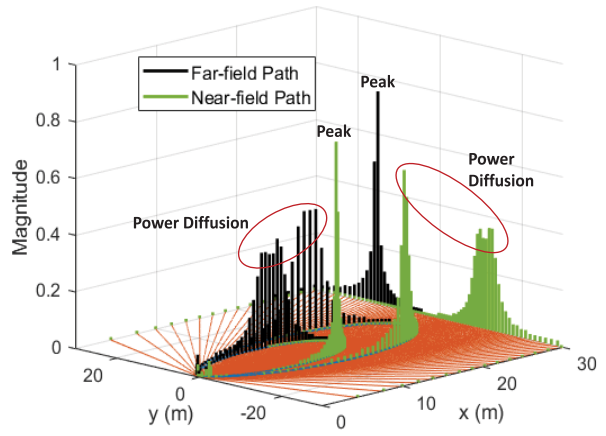

Fig. 7. The channel representation $\mathbf{h}_{J,H}$ in the joint angular-polar domain.

diffusion range are mistaken as two paths, and far-field path 1 is omitted by OMP.

B. Joint Angular-Polar Channel Transform

To solve the issue of inaccurate transform-domain path component estimation, we transform the hybrid-field channel to the joint angular-polar domain. Based on this domain, the information of both far-field and near-field paths can be explicitly extracted to eliminate the influence of the power diffusion effect. The hybrid-field channel representation $\mathbf{h}_{J,H}$ in the joint angular-polar domain is denoted as

$$\mathbf{h}_H = \mathbf{F}_J \mathbf{h}_{J,H}. \tag{20}$$

By defining $\mathbf{F}_A, \mathbf{F}_{P,1}, \mathbf{F}_{P,2} \ldots \mathbf{F}_{P,S}$ as the submatrix of $\mathbf{F}_J$, the joint angular-polar domain transform matrix $\mathbf{F}_J$ can be expressed as [28]

$$\mathbf{F}_J = [\mathbf{F}_A, \mathbf{F}_{P,1}, \mathbf{F}_{P,2} \ldots \mathbf{F}_{P,S_P}]. \tag{21}$$

The far-field and near-field steering vectors contained in $\mathbf{F}_J$ are illustrated in Fig. 6.

Based on $\mathbf{h}_H$, the joint angular-polar domain channel representation of the hybrid-field channel is obtained by

$$\mathbf{h}_{J,H} = |\mathbf{F}_J^H \mathbf{h}_H|. \tag{22}$$

An example of a two-path hybrid-field channel representation $\mathbf{h}_{J,H}$ is shown in Fig. 7. Based on Fig. 7, we obtain the following two observations.

Observation 1: Based on the joint angular-polar domain transform matrix $\mathbf{F}_J$, for each of the L path components, a peak in the joint angular-polar domain corresponding to this path exists.

Observation 2: In the joint angular-polar domain channel representation, for each peak, the magnitude of its peak is larger than the magnitude of its power diffusion counterpart. This is because, among all steering vectors in $\mathbf{F}_J$, the steering vector representing the peak is most correlated with the steering vector representing the path.

Based on the above observations, a novel channel estimation method involving $\hat{L}$ iterations is developed. Specifically, in the l-th iteration, given Observation 1 and Observation 2, a steering vector representing the peak can be found in the joint angular-polar domain channel representation, indicating that a path component is detected. Thus, the estimation of the direction and distance of this path is obtained, and the power diffusion range of the detected path (shown as red ellipses in Fig. 7) can be further determined via calculation, which will be described in Section IV. By identifying and eliminating the interference caused by steering vectors within the power diffusion range of the previously detected paths, the $(l+1)$-th iteration can be performed to detect the corresponding steering vector without being influenced by the power diffusion. Consequently, this approach resolves the issue of inaccurate transform-domain path component estimation and provides a high-resolution approximation for the joint angular-polar domain channel representation $\hat{\mathbf{h}}_J$, thereby enhancing the channel estimation accuracy. The details of the proposed channel estimation method will be elaborated in Section IV.

IV. Hybrid-Field Channel Estimation Algorithm

In this section, we first propose a hybrid-field channel estimation algorithm without prior knowledge of the respective numbers of near-field and far-field paths. We then analyze the computational complexity of the algorithm and the Cramér-Rao Lower Bound (CRLB) of the channel estimation problem in the form of sparse signal recovery.

A. Algorithm Design

We design a new hybrid-field power-diffusion-aware OMP channel estimation algorithm (PD-OMP), which considers the aforementioned power diffusion effect to improve estimation accuracy. The key procedures of PD-OMP are performed in iteration as follows.

1) Path detection (Step 4): Identify the steering vector that exhibits the highest correlation with the residual pilot signal $\mathbf{R}$ for detecting a path. $\mathbf{R}$ is obtained by subtracting the projection of detected paths from the received pilot signal.
2) Power diffusion range identification (Step 5): Generate the power diffusion range of the newly detected path.
3) Residual signal update (Steps 6-8): Eliminate the projection of the newly detected path in the residual signal. The identified power diffusion effect is also removed.

1) Initialization: The PD-OMP is first initialized in Steps 1-3. In Step 1, to explicitly reveal the peaks of all far-field and near-field path components of the hybrid-field multipath channel, we generate the transform matrix $\mathbf{F}_J$ for the joint angular-polar domain according to its definition in (21).

Algorithm 1 Hybrid-Field Channel Estimation Using PD-OMP

Input: Received pilot signal $\mathbf{y}$, power diffusion detection threshold α, number of submatrices S_P of $\mathbf{F}_P$, total number of paths $\hat{L}$, beamforming matrix $\mathbf{W}$.

1: **Step 1**. Generate the hybrid-field transform matrix $\mathbf{F}_J$ with S based on (21).
2: **Step 2**. Calculate the pre-whitening matrix $\mathbf{D}$.
3: **Step 3**. Set the equivalent measurement matrix as $\mathbf{\Phi} = \mathbf{D}^{-1}\mathbf{W}\mathbf{F}_H$. Initialize the support set $\Gamma = \{\emptyset\}$ and the residual signal $\mathbf{R} = \mathbf{D}^{-1}\mathbf{y}$.
4: **for** $l = 1, 2, \ldots, \hat{L}$ **do**
5: **Step 4**. Detect the i_l^*-th steering vector to represent path l based on (26) and obtain the corresponding direction and distance $\{\theta_{i_l^*}, r_{i_l^*}\}$.
6: **Step 5**. Generate the power diffusion range Γ_l for path l with **Algorithm 2**.
7: **Step 6**. Update the support set $\Gamma = \Gamma \cup \Gamma_l$.
8: **Step 7**. Estimate the sparse channel representation $\hat{\mathbf{h}}_{J,H} = \{\mathbf{\Phi}(:, \Gamma)\}^{\dagger}\mathbf{y}$.
9: **Step 8**. Update the residual signal as (27).
10: **end for**
11: **Step 9**. Compute the estimated CSI as (28).

Output: The estimated CSI $\hat{\mathbf{h}_H}$.

We notice that the noise $\mathbf{n}$ in the received pilot signal is time-correlated because of the analog beamforming at the BS. Consequently, after being transformed to the joint angular-polar domain, the power of noise is unevenly distributed among the steering vectors in $\mathbf{F}_J$. In this way, a false projection $\hat{\mathbf{h}}_{J,H}$ of the received pilot signal on the steering vectors in $\mathbf{F}_J$ will be calculated in Step 7 of PD-OMP, which results in an inaccurate channel estimation. Therefore, a noise whitening procedure to generate a time-uncorrelated noise is applied in Step 2 and Step 3. In Step 2, to whiten the noise in the received signal, we calculate the pre-whitening matrix $\mathbf{D}$ based on the beamforming matrix. To be specific, $\mathbf{D}$ is obtained by decomposing the covariance matrix of noise with Cholesky factorization, which is denoted as,

$$\mathbf{C} = \sigma^2 \mathbf{D}\mathbf{D}^H. \tag{23}$$

The covariance matrix of noise is computed as [38]

$$\mathbf{C} = \sigma^2 \mathbb{B}(\mathbf{W}_1\mathbf{W}_1^H, \mathbf{W}_2\mathbf{W}_2^H, \ldots, \mathbf{W}_Q\mathbf{W}_Q^H), \tag{24}$$

where $\mathbb{B}(\cdot)$ represents the generation of a block diagonal matrix and $\mathbf{W}_q$ is the beamforming matrix of the q-th time slot.

In Step 3, we set the equivalent measurement matrix as

$$\mathbf{\Phi} = \mathbf{D}^{-1}\mathbf{W}\mathbf{F}_J, \tag{25}$$

where $\mathbf{\Phi}$ transforms the pilot signal to the joint angular-polar domain in Step 4.

2) Main Body: After the initialization stage, $\hat{L}$ iterations are performed to find the steering vectors corresponding to $\hat{L}$ path components[2] Specifically, in Step 4, we first transform the residual signal to the joint angular-polar domain and then detect a new steering vector as

$$i_l^* = \arg\max_i |\mathbf{\Phi}(:, i)^H \mathbf{R}|^2, \tag{26}$$

which indicates that the residual signal $\mathbf{R}$ has the strongest correlation with the i_l^*-th steering vector in $\mathbf{F}_J$. In this way, a path is detected, and we would like to point out that the direction and distance $\{\theta_{i_l^*}, r_{i_l^*}\}$ associated with the i_l^*-th steering vector is the estimation result for the propagation direction and distance of the newly detected path.

Given $\{\theta_{i_l^*}, r_{i_l^*}\}$ as well as the power of the newly detected path, the power diffusion range Γ_l of this path is generated using **Algorithm 2** in Step 5, which will be presented in Section IV-A3. The overall support set Γ is then updated with the union of Γ_l in Step 6. The channel representation $\hat{\mathbf{h}}_{J,H}$ is estimated with the least square method in Step 7. The residual signal is updated by removing the projection of the detected paths in the received pilot signal in Step 8 as

$$\mathbf{R} = \mathbf{y} - \mathbf{\Phi}(:, \Gamma)\hat{\mathbf{h}}_{J,H}. \tag{27}$$

In this way, the power of the already detected paths, including the diffused power of these paths, is first estimated based on the least square method as $\{\mathbf{\Phi}(:, \Gamma)\}^{\dagger}\mathbf{y}$, and is then removed from the residual pilot signal. The disturbance of the power diffusion effect on channel estimation is eliminated. Finally, in Step 9, the iteration is terminated, and the hybrid-field channel is recovered as

$$\hat{\mathbf{h}_H} = \mathbf{F}_J\hat{\mathbf{h}}_{J,H}. \tag{28}$$

The proposed PD-OMP channel estimation algorithm is summarized in **Algorithm 1**.

3) Identifying the Power Diffusion Range: In Step 5, the power diffusion range of the detected path is generated using **Algorithm 2**. Specifically, the coherence between two steering vectors that are close to each other in direction is generally larger than the coherence between two steering vectors that differ greatly from each other in direction. Hence, to reduce the computational complexity of calculating the coherence, we start by computing the coherence between the i_l^*-th steering vector and the steering vector which is in each submatrix of $\mathbf{F}_J$ and has the same direction as the i_l^*-th steering vector, i.e., the permitted variation in direction $\Delta i = 0$. Each submatrix of $\mathbf{F}_J$ represents a way of sampling the space with a series of

Algorithm 2 Power Diffusion Range Generation for Path l

Input: Hybrid-field transform matrix $\mathbf{F}_J$, the normalized magnitude and steering vector index of the l-th path $\{\bar{m}_l, i_l^*\}$, power diffusion detection threshold α.

1: **Initialize** the power diffusion range $\Gamma_l = \{\emptyset\}$.
2: **for** $s = 0, 1, \ldots, S_P$ **do**
3: **for** $\Delta i = 0, 1, \ldots, M/2$ **do**
4: $i_1 = sM + \mathrm{mod}_M(i_l^* + \Delta i)$.
5: $i_2 = sM + \mathrm{mod}_M(i_l^* - \Delta i)$.
6: $\mu_1 = |\mathbf{F}_j(:, i_l^*)^H \mathbf{F}_j(:, i_1)|$.
7: $\mu_2 = |\mathbf{F}_j(:, i_l^*)^H \mathbf{F}_j(:, i_2)|$.
8: **if** $\mu_1 \geq \alpha/\bar{m}_l$ **then** $\Gamma_l = \Gamma_l \cup \{i_1\}$.
9: **if** $\mu_2 \geq \alpha/\bar{m}_l$ **then** $\Gamma_l = \Gamma_l \cup \{i_2\}$.
10: **if** $\mu_1 < \alpha/\bar{m}_l$ and $\mu_2 < \alpha/\bar{m}_l$ **then** Break.
11: **end for**
12: **end for**

Output: Power diffusion range Γ_l for the path l.

[2] $\hat{L}$ is a typical value of the total number of multipath components and does not necessarily equal the real L. The value of $\hat{L}$ can be chosen based on different scenarios and operating frequency bands [39], [40].

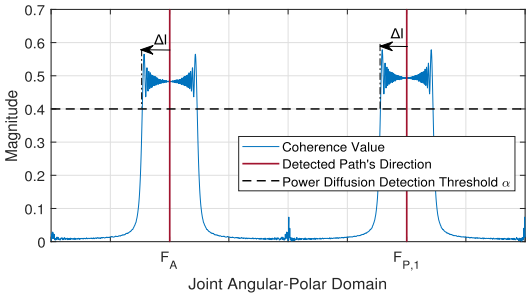

Fig. 8. The illustration of power diffusion range generation based on Algorithm 2.

steering vectors. The criterion for checking whether the i-th steering vector is in the power diffusion range is given as

$$\mu_{i_l^*,i} \geq \frac{\alpha}{\bar{m}_l}, \tag{29}$$

where α is the power diffusion detection threshold and $0 \leq \alpha \leq 1$. $\mu_{i_l^*,i}$ is the coherence between the i-th and i_l^*-th steering vectors. $\bar{m}_l$ is the normalized magnitude of the l-th detected path and is defined as

$$\bar{m}_l = \frac{m_l}{\max_l m_l} = \frac{m_l}{m_1} = \frac{\max_i \left|\mathbf{\Phi}(:,i)^H \mathbf{R}\right|}{m_1}, \tag{30}$$

where m_1 is the magnitude of the first detected path.[3] The magnitude of each path is normalized and is introduced into (29) because the magnitude variation of each path should be considered to limit the power diffusion range of weak paths. If a steering vector satisfies (29), this steering vector carries information about the detected path and is therefore added to the power diffusion range. To generate the complete power diffusion range, the permitted variation in direction, represented as Δi, expands in each submatrix until it violates the criterion (29), as shown in Fig. 8. After we iterate through all the submatrix of $\mathbf{F}_J$, the power diffusion range for the detected path is generated with a smaller computational complexity than calculating the coherence between the i_l^*-th steering vector and each steering vector in $\mathbf{F}_J$.

Based on (29), a smaller α indicates a wider power diffusion range is considered. On the one hand, by applying a large α, the steering vector representing a path with magnitude is likely overlooked. On the other hand, small α gives rise to an extensive power diffusion range, which introduces noise into the estimation result. Therefore, a trade-off of channel estimation accuracy exists for α. The relationship between α and the size of the power diffusion range will be analyzed in Section IV-C, and the effect of α on the performance of PD-OMP will be investigated through simulation in Section V-G.

B. Computational Complexity Analysis

The computational complexity of **Algorithm 1** mainly comes from Step 5 and Step 7. The size of matrices or vectors used in PD-OMP is given as $\mathbf{D} \in \mathbb{C}^{N_{RF} \times N_{RF}}$, $\mathbf{\Phi} \in \mathbb{C}^{QN_{RF} \times M(S_P+1)}$, $\mathbf{R} \in \mathbb{C}^{QN_{RF} \times 1}$, $\mathbf{y} \in \mathbb{C}^{QN_{RF} \times 1}$ and $\hat{\mathbf{h}}_J \in \mathbb{C}^{M(S_P+1) \times 1}$.

[3]Since PD-OMP detects the steering vector with the largest magnitude in each iteration, $\max_l m_l = m_1$.

For Step 3, because the matrix inversion can be performed offline, we focus on the complexity of matrix production, which is $\mathcal{O}((QN_{RF})^2)$. The complexity for Step 4, including the matrix product and the maximizing operation, is $\mathcal{O}(M\hat{L}(S_P+1)(QN_{RF}+1))$. For Step 5, the computational complexity for coherence calculation is $\mathcal{O}(N)$. Hence, the process of power diffusion range generation requires a complexity of $\mathcal{O}(N\text{card}(\Gamma))$, where $\text{card}(\cdot)$ denotes the number of elements for a given set. Step 6 has a $\mathcal{O}(\hat{L})$ complexity. Step 7, 8, 9 have the computational complexity of $\mathcal{O}(QN_{RF}(\text{card}(\Gamma))^2)$, $\mathcal{O}(QN_{RF}\text{card}(\Gamma))$ and $\mathcal{O}(M\text{card}(\Gamma))$, respectively, in each iteration. Considering the large dimension of the antenna array, we have $N > QN_{RF}$. The computational complexity of PD-OMP is $\mathcal{O}((S_P+1)M\hat{L}QN_{RF}) + \mathcal{O}(N\text{card}(\Gamma)) + \mathcal{O}(QN_{RF}\hat{L}(\text{card}(\Gamma))^2)$.

C. Power Diffusion Range Analysis

Since the size of the power diffusion range, i.e., $\text{card}(\Gamma)$, directly affects the computational complexity of PD-OMP, we analyze the influence of power diffusion detection threshold α on $\text{card}(\Gamma)$. A closed-form relationship between $\text{card}(\Gamma)$ and α is intractable because the criterion (29) needs to be checked for each steering vector in the transform matrix $\mathbf{F}_J$ to generate Γ. Since the total power diffusion range can be approximated by the sum of the power diffusion range of each path component in each submatrix, i.e.,

$$\text{card}(\Gamma) \approx \sum_{l=1}^{L} \sum_{s=0}^{S_P} \text{card}(\Gamma_{l,s}), \tag{31}$$

we can obtain an approximation for $\text{card}(\Gamma_{l,s})$ as follows.

Lemma 1: If a path component, which is represented by a steering vector $\mathbf{b}(\theta_p, r_p)$, is transformed based on a submatrix $\mathbf{F}_{J,s} = [\mathbf{b}(\theta_1, r_{s,1}), \mathbf{b}(\theta_2, r_{s,2}), \ldots, \mathbf{b}(\theta_M, r_{s,M})]$, the sum of squares of all transform result components $\left|\mathbf{b}(\theta_m, r_{s,m})^H \mathbf{b}(\theta_p, r_p)\right|, m = 1, 2, \ldots, M$ approximates to 1 if $M = N$. In other words, the transform-domain representation of this path component satisfies

$$\sum_{m=1}^{M} \left|\mathbf{b}(\theta_m, r_{s,m})^H \mathbf{b}(\theta_p, r_p)\right|^2 \approx 1, M = N. \tag{32}$$

Proof: See Appendix A. □

Proposition 1: The size of a power diffusion range for a path l, i.e., $\text{card}(\Gamma_l)$, can be approximated as a piece-wise function of α:

$$\text{card}(\Gamma_l) \approx \sum_{s=-S_0+1}^{S_P-S_0+1} \frac{\epsilon(\bar{m}_l \mu_l(s) - \alpha)}{(\mu_l(s))^2}, \tag{33}$$

where $\epsilon(x) = 1$ if $x \geq 0$ and $\epsilon(x) = 0$ if $x < 0$. Here S_0 is the index of the submatrix containing the detected i_l^*-th steering vector obtained by (26), and $\mu_l(s)$ is the coherence between two steering vectors that are in the same direction but are in the submatrices of $\mathbf{F}_{J,S_0}$ and $\mathbf{F}_{J,S_0+s}$, respectively:

$$\mu_l(s) = \frac{1}{N} \left| \sum_{(1-N)/2}^{(N-1)/2} e^{jkn^2 d^2 s\rho} \right|, \tag{34}$$

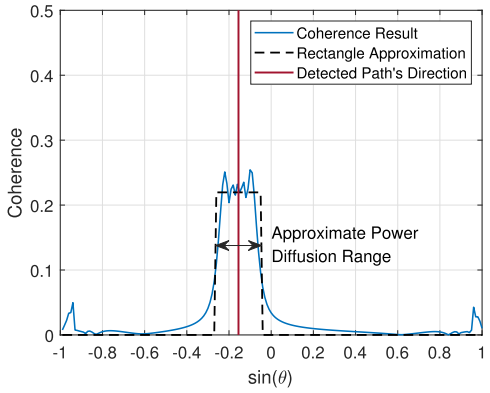

Fig. 9. The illustration of the rectangle approximation of power diffusion range.

where ρ is a parameter for polar-domain transform matrix design.

Proof: According to the simulation result shown in Fig. 9, the power of a detected path concentrates on a few steering vectors around the direction of the detected path. Hence, we apply a rectangle to approximate the power diffusion effect in the $(s-S_0)$-th submatrix such that $\text{card}(\Gamma_{l,s})$ is approximately equal to the width of the rectangle ΔD. We set the steering vector, which has the same direction as the detected i_l^*-th steering vector, to be the midpoint of the rectangle. The height of the rectangle is therefore set as $\mu_l(s)$. According to **Lemma** 1, we have

$$\begin{aligned}\text{card}(\Gamma_{l,s}) \approx \Delta D &\approx \frac{1}{(\mu_l(s))^2}\sum_{m=1}^{M}\left|\mathbf{b}(\theta_m, r_{s,m})^H\mathbf{b}(\theta_p, r_p)\right|^2 \\ &\approx \frac{1}{(\mu_l(s))^2}.\end{aligned} \tag{35}$$

Since the normalized magnitude of each path is considered in the criterion of power diffusion range (29), condition $\bar{m}_l\mu_l(s) \geq \alpha$ is introduced to limit the power diffusion range, which concludes the proof. □

Based on **Proposition** 1, if $M = N$, the relationship between the support set Γ and the power diffusion detection threshold α is given as

$$\text{card}(\Gamma) \approx \sum_{l=1}^{L}\sum_{s=-S_0+1}^{S_P-S_0+1}\frac{\epsilon(\bar{m}_l\mu_l(s)-\alpha)}{(\mu_l(s))^2}. \tag{36}$$

D. Cramér-Rao Lower Bound Analysis

The CRLB bound serves as a theoretical lower bound of MSE to evaluate the performance of channel estimation algorithms. We first derive the CRLB for the estimation of sparse channel representation $\hat{\mathbf{h}}_{J,H}$. Then we obtain the CRLB for the spatial-domain hybrid-field channel $\hat{\mathbf{h}}_H$ based on $\hat{\mathbf{h}}_H = \mathbf{F}_J\hat{\mathbf{h}}_{J,H}$.

Lemma 2: The CRLB for the estimation of sparse channel representation $\hat{\mathbf{h}}_J$ is given as [41]

$$\mathbb{E}\left\{\|\hat{\mathbf{h}}_{J,H}-\mathbf{h}_{J,H}\|_2^2\right\} = \sigma^2\text{Tr}\left(\left(\mathbf{\Phi}_{\mathbf{h}_{J,H}}^H\mathbf{\Phi}_{\mathbf{h}_{J,H}}\right)^{-1}\right), \tag{37}$$

where $\mathbf{\Phi}_{\mathbf{h}_{J,H}} \in \mathcal{C}^{QN_{RF}\times\text{card}(\Gamma)}$ is a matrix composed of columns of $\mathbf{\Phi}$ indexed by the indices of true support set of $\mathbf{h}_{J,H}$.

Since $\text{Rank}(\mathbf{\Phi}_{\mathbf{h}_{J,H}}^H\mathbf{\Phi}_{\mathbf{h}_{J,H}}) = \text{card}(\Gamma)$, (37) can be further written as

$$\text{Tr}\left(\left(\mathbf{\Phi}_{\mathbf{h}_{J,H}}^H\mathbf{\Phi}_{\mathbf{h}_{J,H}}\right)^{-1}\right) = \sum_{i=1}^{\text{card}(\Gamma)}\lambda_i^{-1}, \tag{38}$$

where $\lambda_1, \lambda_2, \ldots \lambda_{\text{card}(\Gamma)}$ are the eigenvalues of $\mathbf{\Phi}_{\mathbf{h}_{J,H}}^H\mathbf{\Phi}_{\mathbf{h}_{J,H}}$.

The coherence of $\mathbf{\Phi}$ is defined as

$$\mu_{\mathbf{\Phi}} = \max_{i\neq j}|\boldsymbol{\phi}_i^H\boldsymbol{\phi}_j|, \tag{39}$$

where $\boldsymbol{\phi}_i$ and $\boldsymbol{\phi}_j$ are the i-th and j-th column of $\mathbf{\Phi}$, respectively, and have the following forms:

$$\boldsymbol{\phi}_i = \mathbf{D}^{-1}\mathbf{W}\mathbf{f}_i, \tag{40}$$

$$\boldsymbol{\phi}_j = \mathbf{D}^{-1}\mathbf{W}\mathbf{f}_j, \tag{41}$$

where $\mathbf{f}_i$ and $\mathbf{f}_j$ are the i-th and j-th column of $\mathbf{F}_J$, respectively. According to the Gershgorin Disc Theorem [42] as well as the fact that $\mathbf{\Phi}_{\mathbf{h}_{J,H}}^H\mathbf{\Phi}_{\mathbf{h}_{J,H}}$ is a positive semidefinite matrix, the eigenvalues of $\mathbf{\Phi}_{\mathbf{h}_{J,H}}^H\mathbf{\Phi}_{\mathbf{h}_{J,H}}$ are real and lie in the range of $[\max\{1-\text{card}(\Gamma)\mu_{\mathbf{\Phi}}, 0\}, 1+\text{card}(\Gamma)\mu_{\mathbf{\Phi}}]$. Therefore, we have

$$\mathbb{E}\left\{\|\hat{\mathbf{h}_{J,H}}-\mathbf{h}_{J,H}\|_2^2\right\} \geq \frac{\sigma^2\text{card}(\Gamma)}{1+\text{card}(\Gamma)\mu_{\mathbf{\Phi}}}. \tag{42}$$

Since $\boldsymbol{\phi}_i$ and $\boldsymbol{\phi}_j$ is obtained by the randomly generated beamforming matrix $\mathbf{W}$, as shown in (40) and (41), $\mu_{\mathbf{\Phi}}$ is a random variable with respect to $\mathbf{W}$. Here, we derive an upper bound on the expectation of $\mu_{\mathbf{\Phi}}$.

Lemma 3: The upper bound for the expectation of $\mu_{\mathbf{\Phi}}$ with respect to $\mathbf{W}$ is given as,

$$\mathbb{E}\{\mu_{\mathbf{\Phi}}\} < \frac{QN_{RF}}{N}. \tag{43}$$

Proof: See Appendix B. □

Based on **Lemma**. 3, we have

$$\begin{aligned}&\mathbb{E}\left\{\|\hat{\mathbf{h}}_{J,H}-\mathbf{h}_{J,H}\|_2^2\right\} \\ &\geq \frac{\sigma^2\text{card}(\Gamma)}{1+\text{card}(\Gamma)\mu_{\mathbf{\Phi}}} \\ &\approx \frac{\sigma^2\text{card}(\Gamma)}{1+\text{card}(\Gamma)\mathbb{E}\{\mu_{\mathbf{\Phi}}\}} > \frac{\sigma^2\text{card}(\Gamma)}{1+\frac{\text{card}(\Gamma)QN_{RF}}{N}}.\end{aligned} \tag{44}$$

Given $\mathbf{h}_H = \mathbf{F}_J\mathbf{h}_{J,H}$, we have the following proposition.

Proposition 2: The CRLB for the estimated hybrid-field multipath channel $\hat{\mathbf{h}}$ is given as

$$\mathbb{E}\left\{\|\hat{\mathbf{h}}_H-\mathbf{h}_H\|_2^2\right\} \geq \frac{\sigma^2\text{card}(\Gamma)}{1+\frac{\text{card}(\Gamma)QN_{RF}}{N}}(\sigma_{\min}(\mathbf{F}_J))^2, \tag{45}$$

where $\sigma_{\min}(\mathbf{F}_J)$ denotes the smallest singular value of $\mathbf{F}_J$.

Proof: See Appendix C. □

Based on the above formula for CRLB, it is observed that the increase in the number of RF chains and pilot length can reduce the CRLB. This is reasonable as additional RF chains and pilot signals can provide more information on the hybrid-field channel, thus improving the estimation accuracy. Besides,

the increase in antenna numbers, which indicates that more parameters must be estimated, increases the CRLB. The rise in power diffusion range size $\mathrm{card}(\Gamma)$ also increases the CRLB.

V. Simulation Results

In this section, we evaluate the performance of our proposed channel estimation algorithm PD-OMP in terms of the normalized mean square error (NMSE). The NMSE is defined as

$$\mathrm{NMSE} = \mathbb{E}\left\{\frac{\|\hat{\mathbf{h}}_H - \mathbf{h}_H\|_2^2}{\|\mathbf{h}_H\|_2^2}\right\}, \tag{46}$$

which is the expectation of the square of the relative estimation error. Besides, the influence of power diffusion detection threshold α on the performance of PD-OMP is investigated.

A. Parameter Setting

In the simulation, we consider the case where an antenna array at the working frequency of 30 GHz is equipped with 200 antenna elements, and the element spacing is set as $d = \lambda/4$ or $d = \lambda/8$. The number of RF chains is set as $N_{RF} = 10$. The number of paths in the multipath channel is set as $L = 7$. The distance and angle of the user and scatterers to the origin satisfy the uniform distribution. The distance for near-field and far-field scatterers are within the range of $(10m, 50m)$ and $(200m, 300m)$, respectively. The angle of all paths are within the range of $(-60°, 60°)$. The joint factor of channel fading and scattering g_l of NLoS path satisfies circularly symmetric complex Gaussian distribution of $\mathcal{CN}(0, 1)$. For the LoS path, $g_l = 1$. Each element of the beamforming matrix $\mathbf{W}$ is randomly chosen from $\{\frac{1}{\sqrt{N}}, -\frac{1}{\sqrt{N}}\}$ with equal probability. The number of submatrices is set as $S_P = 4$. The power diffusion detection threshold α reaching the minimum NMSE is chosen in the simulation.

In the simulation, we calculate the normalized CRLB of CS-based hybrid-field channel estimation, which is denoted as

$$\mathrm{CRLB} = \frac{\sigma^2 \mathrm{card}(\Gamma)}{(1 + \frac{\mathrm{card}(\Gamma) Q N_{RF}}{N})\|\mathbf{h}_H\|_2^2}. \tag{47}$$

To evaluate the performance of PD-OMP, we also compare it with the basic MMSE algorithm and five OMP-based channel estimation algorithms, i.e.,

1) *MMSE* [23]: A basic estimation method that applies the SNR and the spatial correlation matrix to minimize the mean square error of channel estimation.
2) *NPD-OMP* [28]: Estimate the far-field and near-field path components simultaneously with joint angular-polar domain transform.
3) *Far-OMP* [31]: Only apply the far-field angular-domain transform (9). The polar-domain transform is not considered compared with PD-OMP.
4) *HF-OMP* [21]: Require the numbers of near-field and far-field paths as prior information. The far-field path components are estimated first, then near-field path components are estimated.
5) *SD-OMP* [25]: Require the numbers of near-field and far-field paths as prior information. The far-field path components are estimated first. Then, near-field path components are estimated. The far-field path power diffusion is considered because SD-OMP includes additional E far-field steering vectors whose directions are close to the detected far-field steering vector's direction in OMP.

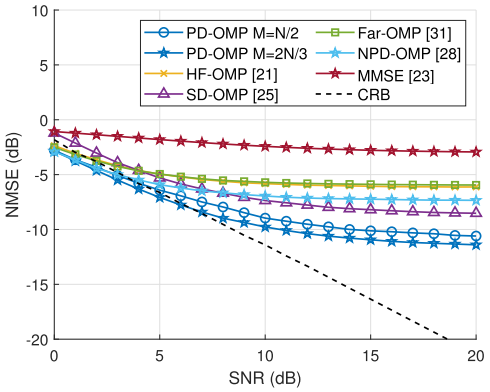

Fig. 10. The NMSE performance versus SNR. Antenna spacing $d = \lambda/4$.

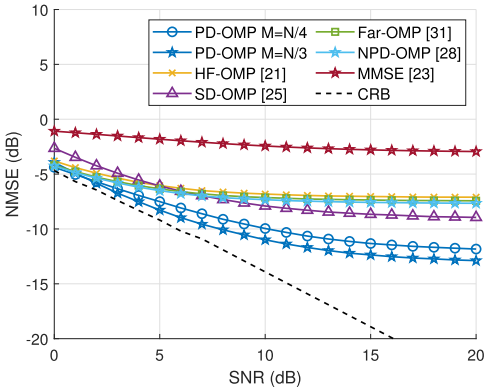

Fig. 11. The NMSE performance versus SNR. Antenna spacing $d = \lambda/8$.

It should be noted that none of the comparing algorithms consider the power diffusion effect in different submatrices as proposed in PD-OMP. The path spilt ratio is set as 0.5 for HF-OMP and SD-OMP.

B. Influence of SNR on Algorithm Performance

Fig. 10 and Fig. 11 demonstrate the NMSE performance of different estimation algorithms versus SNR for antenna spacing $d = \lambda/4$ and $d = \lambda/8$, respectively. Compared with HF-OMP or SD-OMP, which requires the numbers of near-field and far-field paths as prior knowledge, PD-OMP can estimate the channel more accurately without the prior knowledge of path distribution, demonstrating the effectiveness of the proposed algorithm. This is because PD-OMP applies the joint angular-polar transform matrix, which can capture both the far-field and near-field features of the channel. The NMSE of PD-OMP is lower than that of NPD-OMP, which shows the necessity of considering the power diffusion range in the support set. Besides, PD-OMP enjoys superiority over benchmark algorithms when the SNR is closer to 20 dB. This is because, at a higher SNR, the power diffusion range can be estimated more accurately, which PD-OMP then utilizes to compensate

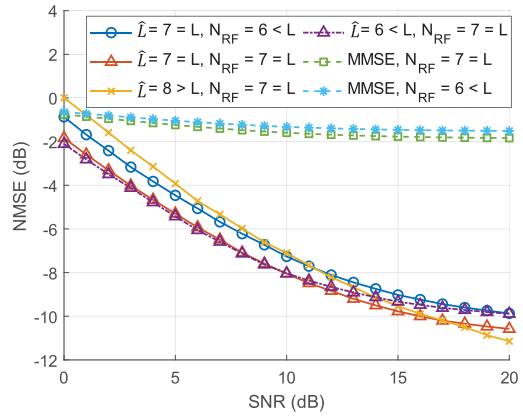

Fig. 12. The NMSE versus SNR for different $\hat{L}$ and different N_{RF}.

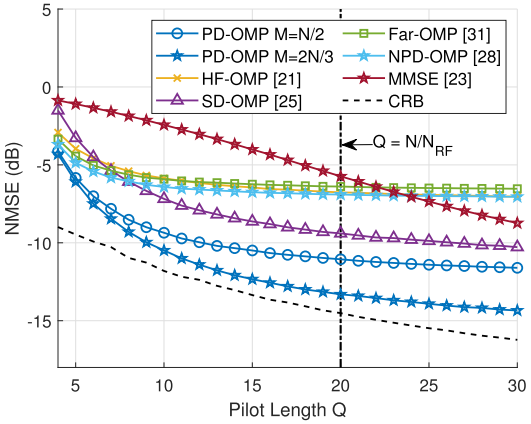

Fig. 13. The NMSE performance versus the pilot length Q. Antenna spacing $d = \lambda/4$.

for the performance degradation caused by the power diffusion effect. In contrast, none of the existing algorithms consider the power diffusion effect. Moreover, an enhancement in accuracy is obtained by using the overcomplete dictionary rather than the orthonormal basis in PD-OMP.

We also calculate the CRLB to evaluate the theoretical performance of PD-OMP. We observe that in Fig. 10 CRLB is larger than the NMSE when SNR ≤ 8 dB, which shows that CRLB is valid for PD-OMP only at a high SNR regime. This is because CRLB gives a theoretical lower bound for unbiased estimators. However, OMP is a biased estimator [43] and the bias is not negligible at a lower SNR regime.

Fig. 12 demonstrates the NMSE performance of proposed PD-OMP for different $\hat{L}$ and different N_{RF}. As can be observed from Fig. 12, increased N_{RF} leads to more accurate channel estimation because more pilot signals can be used for channel estimation with a higher N_{RF}. Besides, when SNR $\geq$ 15 dB, the estimation accuracy is reduced when $\hat{L} < L$ and changes slightly when $\hat{L} > L$. The proposed PD-OMP estimates the channel more accurately than MMSE for $N_{RF} < L$ and $N_{RF} = L$.

C. Influence of Pilot Length on Algorithm Performance

Fig. 13 presents the NMSE performance of different algorithms with the increase of pilot length Q. PD-OMP can achieve the lowest NMSE among all benchmark methods for different Q. In other words, PD-OMP requires a small pilot length to achieve the same estimation accuracy. For instance, to reach an NMSE of -5.8 dB, PD-OMP only requires $Q = 8$ while MMSE requires $Q = 20$. Besides, the gaps of NMSE between PD-OMP and benchmark methods increase with Q. This is because more pilot signals can provide more information on the channel so that for PD-OMP, the power diffusion range can be generated more accurately to help channel estimation.

TABLE I
COMPLEXITY COMPARISON OF DIFFERENT CHANNEL ESTIMATION ALGORITHMS FOR $d = d$

MMSE	$\mathcal{O}(N^3)$
NPD-OMP	$\mathcal{O}(M(S_P+1)N_{RF}Q\hat{L}) + \mathcal{O}(N_{RF}Q\hat{L}^3)$
Far-OMP	$\mathcal{O}(N_{RF}Q\hat{L}^3) + \mathcal{O}(MN_{RF}Q\hat{L})$
HF-OMP	$\mathcal{O}(N_{RF}Q(\hat{L}_n^3 + \hat{L}_f^3))+$ $\mathcal{O}(MN_{RF}Q(S\hat{L}_n + \hat{L}_f))$
SD-OMP	$\mathcal{O}(N_{RF}Q(\hat{L}_n^3(E+1)^3 + \hat{L}_f^2(E+1)^2)+$ $\mathcal{O}(MN_{RF}Q(S_P\hat{L}_n + \hat{L}_f))$
PD-OMP	$\mathcal{O}(N_{RF}Q\hat{L}\text{card}^2(\Gamma))+$ $\mathcal{O}(M(S_P+1)N_{RF}Q\hat{L}) + \mathcal{O}(N\text{card}(\Gamma))$

D. Influence of Scatterer Distribution

The scatterer distribution is defined as the split ratio $\gamma = \text{card}(\mathbb{L}_N)/L$, which represents the ratio of the near-field path numbers $\text{card}(\mathbb{L}_N)$ to the total multipath numbers L. The mean, standard deviation, maximum, and minimum of NMSE concerning γ are applied to evaluate whether algorithms are robust to the variation of the split ratio. The mean and standard deviation of NMSE are calculated by

$$\overline{\text{NMSE}} = \frac{\sum_{\gamma\in\Xi}\text{NMSE}_\gamma}{\text{Card}(\Xi)}, \tag{48}$$

$$\sigma_{\text{NMSE}} = \sqrt{\frac{\sum_{\gamma\in\Xi}(\text{NMSE}_\gamma - \overline{\text{NMSE}})^2}{\text{Card}(\Xi)}}, \tag{49}$$

where $\Xi = \{0, 0.1, \ldots, 1\}$ and NMSE_γ denotes the NMSE performance obtained by PD-OMP given the split ratio γ. The simulation parameters are set as $L = 10$, SNR $= 10$ dB, and $Q = 10$.

It is observed from **Table** II that PD-OMP achieves the lowest mean estimation error among all benchmark algorithms and the lowest standard deviation of estimation error among all OMP-based benchmark algorithms. It is noted that the MMSE method obtains a lower standard deviation than PD-OMP because MMSE employs the statistical information of the channel to assist channel estimation. Besides, the PD-OMP has the smallest maximum NMSE among all methods. Hence, PD-OMP is robust to the change of split ratio in the hybrid-field wireless communication scenario, demonstrating its stability against the scatterer distribution variation.

E. Advantage of Joint Angular-Polar Domain Channel Transform

To demonstrate the necessity of applying joint angular-polar domain channel transform instead of the polar-domain channel

TABLE II
MEAN AND STANDARD DEVIATION OF NMSE WITH RESPECT TO γ FOR DIFFERENT ALGORITHMS

NMSE (dB)	**PD-OMP (Proposed)**	Near-OMP [11]	Far-OMP [18]	HF-OMP [13]	MMSE [29]
Mean	**-6.792 (✓)**	-3.973	-5.899	-5.341	-2.428
Standard Deviation	0.118	0.448	0.537	0.683	**0.020 (✓)**
Range	**[-6.964, -6.646] (✓)**	[-4.862, -3.412]	[-6.800, -5.081]	[-6.800, -4.606]	[-2.395, -2.462]

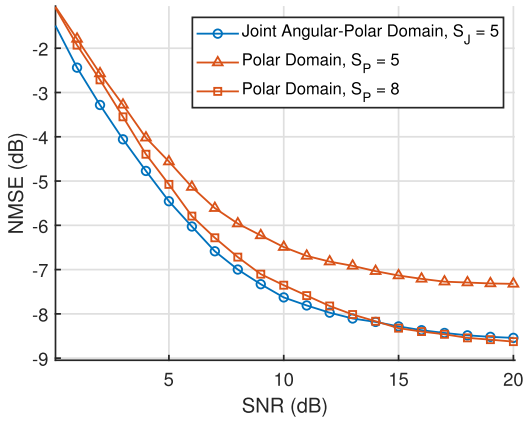

Fig. 14. The NMSE performance of PD-OMP and Near-PD-OMP with different numbers of submatrices in the transform matrix.

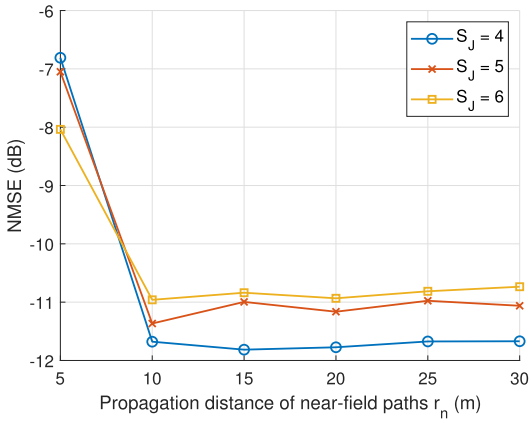

Fig. 15. The NMSE performance versus propagation distances of near-field paths for different S_J.

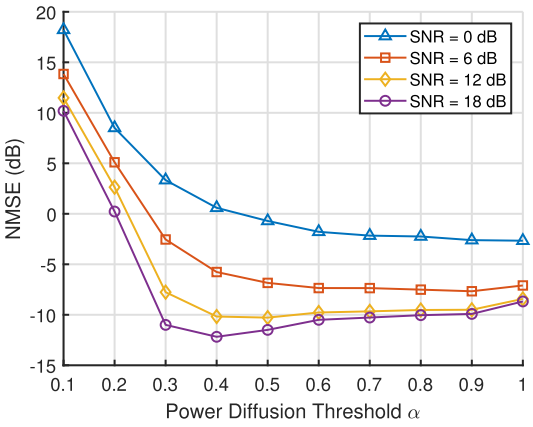

Fig. 16. The NMSE performance of PD-OMP of different α versus SNR.

transform in the hybrid-field channel estimation, we compare the performances of two transforms in Fig. 14. The curves "Polar Domain $S_P = 5$" and "Polar Domain $S_P = 8$" are obtained with a channel estimation method that replaces the joint angular-polar domain transform in PD-OMP with the polar-domain transform. We use S_P and S_J to denote the number of submatrices in the near-field polar domain transform-domain matrix and the joint angular-polar domain transform matrix, respectively. A larger S_P or S_J indicates that a larger area is sampled with near-field steering vectors, which induces a higher computational complexity.

As shown in Fig. 14, when we set $S_J = S_P = 5$ for both transform matrices, i.e., the computational complexity for two algorithms based on different transform matrices are the same, the NMSE of the joint angular-polar domain transform is smaller than the polar-domain transform. Compared with the polar-domain channel transform ($S_P = 8$), the joint angular-polar domain channel transform ($S_J = 5$) saves 37.5% computational complexity while achieving a similar NMSE performance. Hence, the joint angular-polar domain can help balance the estimation accuracy and the computational complexity.

F. Influence of Transform Matrix Design on Algorithm Performance

Here, we analyze the impact of the distance sampling in the joint angular-polar domain on the algorithm performance. According to the distance sampling method (15) for the joint angular-polar domain transform matrix $\mathbf{F}_J$, the increase of submatrices number S_J can enlarge the area to be sampled by $\mathbf{F}_J$, while an increased β_Δ will provide a more densely sampled near-field region.

In Fig. 15, we demonstrate the NMSE performance of PD-OMP versus propagation distances of near-field paths r_n for different numbers of submatrices S_J at SNR $= 15$ dB. $S_J = 6$ can lead to the best estimation accuracy when $r_n = 5\ m$. This is because the region closer to the antenna array is sampled by $\mathbf{F}_J$ as S_J grows. However, for $r_n \geq 10m$, $S_J = 4$ achieves the best estimation accuracy.

G. Influence of Power Diffusion Detection Threshold α on Algorithm Performance

Power diffusion detection threshold $\alpha \in (0, 1]$ decides the considered power diffusion range in PD-OMP, which affects the estimation accuracy and the computational complexity of PD-OMP.

In Fig. 16, how the NMSE of PD-OMP changes with the SNR and the power diffusion detection threshold α is investigated. The NMSE reduces as the SNR increases for

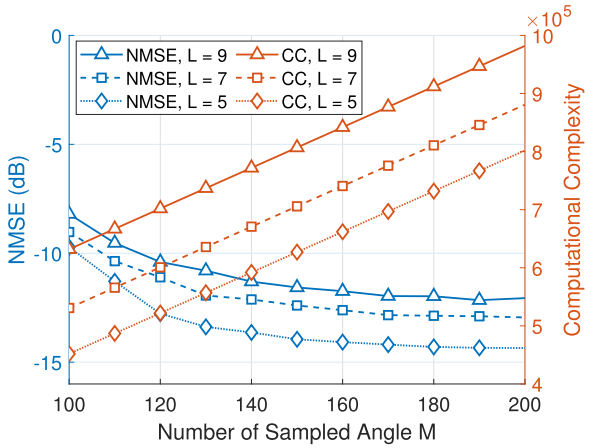

Fig. 17. The NMSE performance and computational complexity versus the number of sampled angles M.

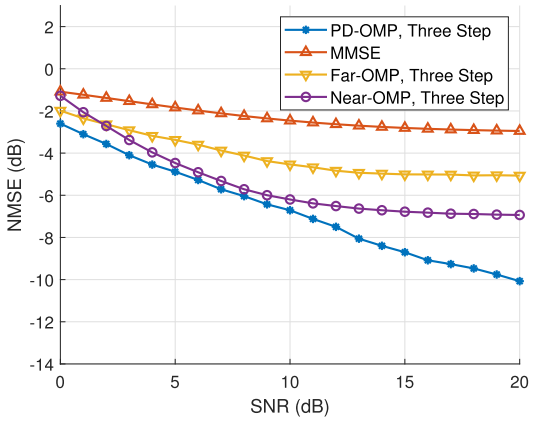

Fig. 18. The NMSE performance versus SNR in the case of planar array channel estimation.

different α. Besides, with the increase of SNR, PD-OMP with a decreased α can achieve the lowest NMSE. This is because the inaccurate transform-domain path component estimation is alleviated by applying a smaller α for a high SNR. However, if the SNR is low, a falsely included power diffusion range will introduce additional noise to the estimation result and worsen the NMSE performance. Therefore, Fig. 16 reveals that when the SNR is low, a high α should be selected to limit the range of power diffusion to improve the channel estimation accuracy.

H. Influence of Sampled Angles M on Algorithm Performance

In Fig.17, we demonstrate the NMSE of PD-OMP and the computational complexity of PD-OMP concerning the number of Sampled Angles $M \in [N/2, N]$. The dimension of computational complexity is based on the analysis in Section IV-B. First, a trade-off between the estimation accuracy and computational complexity is revealed. A higher estimation accuracy is achieved with the increased number of sampled angles. This is because a larger M provides a more refined angle sampling, so the direction of paths is estimated more accurately. Besides, the dimension of computational complexity grows with M. Second, it is observed that with the increase of path number, both computational complexity and NMSE increase. This is because additional paths lead to an increasingly complicated multipath channel, and a wider power diffusion range has to be estimated, which gives rise to higher estimation errors and additional calculations.

I. Extending PD-OMP to Planar Arrays

The proposed PD-OMP can be further extended to the planar array scenario, which can be seen as multiple layers of horizontal linear arrays. Therefore, the channel estimation for a planar array can be decomposed into channel estimation for different linear arrays, and an intuitive three-step estimation method is designed. In Step 1, PD-OMP is performed for each layer independently. In Step 2, the joint sparsity of the channel is exploited, as a scatterer can create path components for each layer. We refine the steering vectors in the support set based on the steering vectors' appearance frequency in the support sets of all layers obtained from Step 1. In Step 3, a least square estimation based on the refined support set is performed to estimate the channel.

Fig. 18 illustrates the NMSE performance of PD-OMP versus SNR in the case of planar array channel estimation, where a 10×100 planar array is considered. It can be observed that the three-step channel estimation method can achieve a higher channel estimation accuracy than baseline algorithms. Besides, compared with the independent estimation result based on Step 1, the support set refinement process is effective in increasing the estimation accuracy for PD-OMP.

VI. Conclusion

In this paper, we investigated the hybrid-field multipath channel estimation in holographic MIMO communications. We first identified the issue of inaccurate path component estimation, which led to inaccurate channel estimation if the conventional far-field or near-field channel estimation methods were applied to the hybrid-field case. We revealed that the reason came from the power diffusion effect that the power of each path diffused to other positions. In consequence, fake paths were generated in the channel representation in transform domains so that path components were difficult to separate from each other. To cope with the power diffusion effect, we transformed the hybrid-field channel from the spatial domain to the joint-angular-polar domain. A solution concept of power diffusion range was introduced to quantify the range of diffused power so that the power diffusion effect could be identified and eliminated. A novel channel estimation algorithm, PD-OMP, was then proposed. The computational complexity of PD-OMP and the CRLB of sparse-signal-recovery-based hybrid-field channel estimation were derived. The theoretical analysis showed that the computational complexity of PD-OMP was linear with the number of antenna elements.

Simulation results showed that: 1) The joint angular-polar domain channel employed by PD-OMP can extract both far-field and near-field path components of the hybrid-field channel effectively. 2) The proposed PD-OMP outperforms current state-of-the-art hybrid-field channel estimation methods under different SNRs and pilot lengths. Besides, PD-OMP was robust to the variation of scatterer distribution. 3) When

the SNR increases, a wider power diffusion range should be selected in PD-OMP to produce a smaller NMSE. 4) There exists an optimal number of sampled angles to reach a trade-off between the computational complexity and the channel estimation accuracy of PD-OMP.

APPENDIX A
PROOF OF LEMMA 1

We omit the propagation direction and transmission distance (θ_p, r_p) of the steering vector $\mathbf{b}(\theta_p, r_p)$ for simplicity. Because we consider the case of $M = N$, we have

$$\sum_{n=1}^{N} \left|\mathbf{b}(\theta_n, r_{s,n})^H \mathbf{b}\right|^2 = (\mathbf{F}_{J,s}^H \mathbf{b})^H \mathbf{F}_{J,s}^H \mathbf{b} = \mathrm{Tr}(\mathbf{F}_{J,s}\mathbf{F}_{J,s}^H \mathbf{b}\mathbf{b}^H), \tag{50}$$

where $\mathbf{F}_{J,s}$ is the s-th submatrix of $\mathbf{F}_J$. The term $\mathbf{F}_{J,s}\mathbf{F}_{J,s}^H$ is denoted as

$$\mathbf{F}_{J,s}\mathbf{F}_{J,s}^H = \begin{pmatrix} \chi_{1,1} & \cdots & \chi_{1,N} \\ \vdots & \ddots & \vdots \\ \chi_{N,1} & \cdots & \chi_{N,N} \end{pmatrix}. \tag{51}$$

The term $\mathbf{b}\mathbf{b}^H$ is denoted as

$$\mathbf{b}\mathbf{b}^H = \frac{1}{N}\begin{pmatrix} e^{-jk(r_{1,p}-r_{1,p})} & \cdots & e^{-jk(r_{1,p}-r_{N,p})} \\ \vdots & \ddots & \vdots \\ e^{-jk(r_{N,p}-r_{1,p})} & \cdots & e^{-jk(r_{N,p}-r_{N,p})} \end{pmatrix}. \tag{52}$$

Therefore, we have

$$\{\mathbf{F}_{J,s}^H \mathbf{F}_{J,s}\mathbf{b}\mathbf{b}^H\}_{j,j} = \frac{1}{N}\sum_{n=1}^{N} \chi_{j,n} e^{-jk(r_{n,p}-r_{j,p})}. \tag{53}$$

Since only one submatrix is considered, we have

$$\chi_{j,n} e^{-jk(r_{n,p}-r_{j,p})} \overset{(a)}{\approx} \tag{54}$$

$$\frac{1}{N}\sum_{z=(1-N)/2}^{(N-1)/2} e^{j\pi z(\sin\theta_j - \sin\theta_n)} e^{-jk(r_{n,p}-r_{j,p})} \overset{j\neq n}{=} \tag{55}$$

$$e^{\frac{j\pi(\sin(\theta_j)-\sin(\theta_n))(1-N)}{2} - jk(r_{n,p}-r_{j,p})} \frac{1-e^{j\pi N(\sin(\theta_j)-\sin(\theta_n))}}{1-e^{j\pi(\sin(\theta_j)-\sin(\theta_n))}}, \tag{56}$$

where the approximation (a) is obtained by performing the second-order Taylor Expansion to the distance term $r_{y,s,j}$ and $r_{y,s,n}$ for each $y = 1, \ldots, N$ in the steering vector $\mathbf{b}(\theta_j, r_{s,j})$ and $\mathbf{b}(\theta_n, r_{s,n})$, which are used in the calculation of $\chi_{j,n}$. The second-order Taylor Expansion for $r_{y,s,j}$ around $r_{s,j}$ is expressed as

$$r_{y,s,j} = r_{s,j} - t_y d\sin(\theta_j) + \frac{t_y^2 d^2(1-\sin^2(\theta_j))}{r_{s,j}}, \tag{57}$$

where $t_y = \frac{2y-N+1}{2}$. Besides, the transform from (54) to (55) also employs the following equation:

$$\frac{1-\sin^2(\theta_j)}{r_{s,j}} = \frac{1-\sin^2(\theta_n)}{r_{s,n}}, \tag{58}$$

which is a property of the joint angular-polar domain transform matrix.

Due to the definition of direction θ in (11), $\sin(\theta_j) - \sin(\theta_n)$ is multiple of $2/N$. Therefore, based on (56), we have

$$\chi_{j,n} e^{-jk(r_{n,p}-r_{j,p})} \approx \begin{cases} 0 & j \neq n, \\ 1 & j = n. \end{cases} \tag{59}$$

Therefore, $\{\mathbf{F}_{J,s}^H \mathbf{F}_{J,s}\mathbf{b}\mathbf{b}^H\}_{j,j} \approx \frac{1}{N}$, and we have

$$\mathrm{Tr}(\mathbf{F}_{J,s}^H \mathbf{F}_{J,s}\mathbf{b}\mathbf{b}^H) \approx N * \frac{1}{N} = 1. \tag{60}$$

APPENDIX B
PROOF OF LEMMA 3

The term $\mu_{\mathbf{\Phi}}$ is expressed as $\mu_{\mathbf{\Phi}} = \max_{i\neq j} |\boldsymbol{\phi}_i^H \boldsymbol{\phi}_j|$, and we have $\boldsymbol{\phi}_i = \mathbf{D}^{-1}\mathbf{W}\mathbf{f}_i$ and $\boldsymbol{\phi}_j = \mathbf{D}^{-1}\mathbf{W}\mathbf{f}_j$, where $\mathbf{f}_i$ and $\mathbf{f}_j$ are the i-th and j-th column of $\mathbf{F}_J$, respectively. Therefore,

$$\begin{aligned} &|\boldsymbol{\phi}_i^H \boldsymbol{\phi}_j| \\ &= |(\mathbf{D}^{-1}\mathbf{W}\mathbf{f}_i)^H \mathbf{D}^{-1}\mathbf{W}\mathbf{f}_j| \\ &= |\mathbf{f}_i^H \mathbf{W}^H (\mathbf{D}^H\mathbf{D})^{-1}\mathbf{W}\mathbf{f}_j| = |\mathbf{W}^H \mathbf{f}_i^H \mathbf{C}^{-1}\mathbf{W}\mathbf{f}_j| \\ &= |\mathbf{f}_i^H \mathbf{W}^H (\mathbb{B}\left\{\mathbf{W}_1\mathbf{W}_1^H, \mathbf{W}_2\mathbf{W}_2^H, \ldots \mathbf{W}_Q\mathbf{W}_Q^H\right\})^{-1}\mathbf{W}\mathbf{f}_j| \\ &= |\mathbf{f}_i^H \mathbf{W}^H (\mathbb{B}\left\{(\mathbf{W}_1\mathbf{W}_1^H)^{-1}, \ldots (\mathbf{W}_Q\mathbf{W}_Q^H)^{-1}\right\})\mathbf{W}\mathbf{f}_j| \\ &= |\mathbf{f}_i^H \sum_{q=1}^{Q}\left\{\mathbf{W}_q^H(\mathbf{W}_q\mathbf{W}_q^H)^{-1}\mathbf{W}_q\right\}\mathbf{f}_j|. \end{aligned} \tag{61}$$

Considering that the beamforming is randomly generated, we further analyze the expectation of $\mu_{\mathbf{\Phi}}$:

$$\begin{aligned} \mathbb{E}\{\mu_{\mathbf{\Phi}}\} &= |\mathbf{f}_i^H \mathbb{E}\left\{\sum_{q=1}^{Q}\left\{\mathbf{W}_q^H(\mathbf{W}_q\mathbf{W}_q^H)^{-1}\mathbf{W}_q\right\}\right\}\mathbf{f}_j| \\ &= Q|\mathbf{f}_i^H \mathbb{E}\left\{\mathbf{W}_q^H(\mathbf{W}_q\mathbf{W}_q^H)^{-1}\mathbf{W}_q\right\}\mathbf{f}_j|, \forall q. \end{aligned} \tag{62}$$

Considering the expectation of the (x, y)-th element of $\mathbf{W}_q\mathbf{W}_q^H$:

$$\mathbb{E}\left\{(\mathbf{W}_q\mathbf{W}_q^H)_{x,y}\right\} = \mathbb{E}\left\{\sum_{z=1}^{N}((\mathbf{W}_q)_{x,z}(\mathbf{W}_q^H)_{z,y})\right\}. \tag{63}$$

Because the modulus of each element of the beamforming matrix $\mathbf{W}_q$ is 1, and each element is independently and randomly chosen with equal probability, we have

$$\mathbb{E}\left\{(\mathbf{W}_q\mathbf{W}_q^H)_{x,y}\right\} = \begin{cases} N, & \text{if } x = y, \\ 0, & \text{if } x \neq y. \end{cases} \tag{64}$$

Identically, considering the expectation of the (x, y)-th element of $\mathbf{W}_q^H\mathbf{W}_q$, we have

$$\mathbb{E}\left\{(\mathbf{W}_q^H\mathbf{W}_q)_{x,y}\right\} = \begin{cases} N_{RF}, & \text{if } x = y, \\ 0, & \text{if } x \neq y. \end{cases} \tag{65}$$

Therefore, we have $\mathbb{E}\left\{\mathbf{W}_q^H(\mathbf{W}_q\mathbf{W}_q^H)^{-1}\mathbf{W}_q\right\} = \frac{N_{RF}}{N}\mathbf{I}_{N\times N}$.

Since the modulus of each element of $\mathbf{f}_i$ is $\frac{1}{\sqrt{N}}$, $\forall i$, we have

$$\mathbb{E}\{\mu_{\mathbf{\Phi}}\} = \frac{QN_{RF}}{N}\max_{i\neq j}|\mathbf{f}_i^H\mathbf{f}_j| < \frac{QN_{RF}}{N}. \tag{66}$$

APPENDIX C
PROOF OF PROPOSITION 2

For an arbitrary matrix $\mathbf{A}$ and an arbitrary vector $\mathbf{x}$,

$$\|\mathbf{A}\mathbf{x}\|_2 \geq \sigma_{\min}(\mathbf{A})\|\mathbf{x}\|_2, \tag{67}$$

where $\sigma_{\min}(\mathbf{A})$ is the minimum singular value of matrix $\mathbf{A}$. Hence, we have

$$\begin{aligned}&\|\hat{\mathbf{h}}_H - \mathbf{h}_H\|_2^2 \\ &= \|\mathbf{F}_J(\hat{\mathbf{h}}_{J,H} - \mathbf{h}_{J,H})\|_2^2 \geq (\sigma_{\min}(\mathbf{F}_J))^2\|(\hat{\mathbf{h}}_{J,H} - \mathbf{h}_{J,H})\|_2^2.\end{aligned} \tag{68}$$

Thus, we have

$$\mathbb{E}\left\{\|\hat{\mathbf{h}}_H - \mathbf{h}_H\|_2^2\right\} \geq (\sigma_{\min}(\mathbf{F}_J))^2 \frac{\sigma^2 \mathrm{card}(\Gamma)}{1 + \frac{\mathrm{card}(\Gamma)QN_{RF}}{N}}. \tag{69}$$

REFERENCES

[1] S. Yue, S. Zeng, L. Liu, and B. Di, "Channel estimation for holographic communications in hybrid near-far field," in *Proc. GLOBECOM IEEE Global Commun. Conf.*, Kuala Lumpur, Malaysia, Dec. 2023, pp. 1–6.

[2] W. Saad, M. Bennis, and M. Chen, "A vision of 6G wireless systems: Applications, trends, technologies, and open research problems," *IEEE Netw.*, vol. 34, no. 3, pp. 134–142, May 2020.

[3] T. Gong et al., "Holographic MIMO communications: Theoretical foundations, enabling technologies, and future directions," *IEEE Commun. Surveys Tuts.*, vol. 26, no. 1, pp. 196–257, 1st Quart., 2024.

[4] R. Deng, B. Di, H. Zhang, and L. Song, "HDMA: Holographic-pattern division multiple access," *IEEE J. Sel. Areas Commun.*, vol. 40, no. 4, pp. 1317–1332, Apr. 2022.

[5] J. An, C. Yuen, C. Huang, M. Debbah, H. V. Poor, and L. Hanzo, "A tutorial on holographic MIMO communications—Part III: Open opportunities and challenges," *IEEE Commun. Lett.*, vol. 27, no. 7, pp. 1674–1678, Jul. 2023.

[6] C. Huang et al., "Holographic MIMO surfaces for 6G wireless networks: Opportunities, challenges, and trends," *IEEE Wireless Commun.*, vol. 27, no. 5, pp. 118–125, Oct. 2020.

[7] J. An, C. Yuen, C. Huang, M. Debbah, H. Vincent Poor, and L. Hanzo, "A tutorial on holographic MIMO communications—Part I: Channel modeling and channel estimation," *IEEE Commun. Lett.*, vol. 27, no. 7, pp. 1664–1668, Jul. 2023.

[8] J. An, C. Yuen, C. Huang, M. Debbah, H. V. Poor, and L. Hanzo, "A tutorial on holographic MIMO communications—Part II: Performance analysis and holographic beamforming," *IEEE Commun. Lett.*, vol. 27, no. 7, pp. 1669–1673, Jul. 2023.

[9] R. Deng, B. Di, H. Zhang, Y. Tan, and L. Song, "Reconfigurable holographic surface: Holographic beamforming for metasurface-aided wireless communications," *IEEE Trans. Veh. Technol.*, vol. 70, no. 6, pp. 6255–6259, Jun. 2021.

[10] D. Dardari, "Communicating with large intelligent surfaces: Fundamental limits and models," *IEEE J. Sel. Areas Commun.*, vol. 38, no. 11, pp. 2526–2537, Nov. 2020.

[11] S. Zeng, H. Zhang, B. Di, Z. Han, and L. Song, "Reconfigurable intelligent surface (RIS) assisted wireless coverage extension: RIS orientation and location optimization," *IEEE Commun. Lett.*, vol. 25, no. 1, pp. 269–273, Jan. 2021.

[12] Y. Han, W. Tang, S. Jin, C.-K. Wen, and X. Ma, "Large intelligent surface-assisted wireless communication exploiting statistical CSI," *IEEE Trans. Veh. Technol.*, vol. 68, no. 8, pp. 8238–8242, Aug. 2019.

[13] B. Di, H. Zhang, L. Song, Y. Li, Z. Han, and H. V. Poor, "Hybrid beamforming for reconfigurable intelligent surface based multi-User communications: Achievable rates With limited discrete phase shifts," *IEEE J. Sel. Areas Commun.*, vol. 38, no. 8, pp. 1809–1822, Aug. 2020.

[14] S. Yue, S. Zeng, H. Zhang, F. Lin, L. Liu, and B. Di, "Intelligent omni-surfaces aided wireless communications: Does the reciprocity hold?" *IEEE Trans. Veh. Technol.*, vol. 72, no. 6, pp. 8181–8185, Jun. 2023.

[15] J. An et al., "Stacked intelligent metasurfaces for efficient holographic MIMO communications in 6G," *IEEE J. Sel. Areas Commun.*, vol. 41, no. 8, pp. 2380–2396, Aug. 2023.

[16] Ö. T. Demir, E. Björnson, and L. Sanguinetti, "Channel modeling and channel estimation for holographic massive MIMO with planar arrays," *IEEE Wireless Commun. Lett.*, vol. 11, no. 5, pp. 997–1001, May 2022.

[17] Y. Liu, Z. Wang, J. Xu, C. Ouyang, X. Mu, and R. Schober, "Near-field communications: A tutorial review," *IEEE Open J. Commun. Soc.*, vol. 4, pp. 1999–2049, 2023.

[18] M. K. Ozdemir, H. Arslan, and E. Arvas, "On the correlation analysis of antennas in adaptive MIMO systems with 3-D multipath scattering," in *Proc. IEEE Wireless Commun. Netw. Conf. (WCNC)*, Atlanta, GA, USA, Mar. 2004, pp. 295–299.

[19] E. Björnson, Ö. T. Demir, and L. Sanguinetti, "A primer on near-field beamforming for arrays and reconfigurable intelligent surfaces," in *Proc. Asilomar Conf. Signals, Syst., Comput. (ACSSC)*, Pacific Grove, CA, USA, Oct. 2021, pp. 105–112.

[20] J. An, C. Yuen, L. Dai, M. Di Renzo, M. Debbah, and L. Hanzo, "Toward beamfocusing-aided near-field communications: Research advances, potential, and challenges," 2023, *arXiv:2309.09242*.

[21] X. Wei and L. Dai, "Channel estimation for extremely large-scale massive MIMO: far-field, near-field, or hybrid-field?" *IEEE Commun. Lett.*, vol. 26, no. 1, pp. 177–181, Jan. 2022.

[22] K. Chen, C. Qi, and C.-X. Wang, "Two-stage hybrid-field beam training for ultra-massive MIMO systems," in *Proc. IEEE/CIC Int. Conf. Commun. China (ICCC)*, Aug. 2022, pp. 1074–1079.

[23] R. W. Heath Jr. and A. Lozano, "Channel estimation," in *Foundations of MIMO Communication*. Cambridge, U.K.: Cambridge Univ. Press, 2019, pp. 116–120.

[24] W. Yu, Y. Shen, H. He, X. Yu, J. Zhang, and K. B. Letaief, "Hybrid far- and near-field channel estimation for THz ultra-massive MIMO via fixed point networks," in *Proc. IEEE Global Commun. Conf.*, Dec. 2022, pp. 5384–5389.

[25] Z. Hu, C. Chen, Y. Jin, L. Zhou, and Q. Wei, "Hybrid-field channel estimation for extremely large-scale massive MIMO system," *IEEE Commun. Lett.*, vol. 27, no. 1, pp. 303–307, Jan. 2023.

[26] S. Tarboush, A. Ali, and T. Y. Al-Naffouri, "Cross-field channel estimation for ultra massive-MIMO THz systems," *IEEE Trans. Wireless Commun.*, early access, Jan. 12, 2024, doi: 10.1109/TWC.2024.3352894.

[27] Y. Chen, Y. Wang, Z. Wang, and Z. Han, "Angular-distance based channel estimation for holographic MIMO," *IEEE J. Sel. Areas Commun.*, vol. 42, no. 6, pp. 1684–1702, Jun. 2024.

[28] M. Cui and L. Dai, "Channel estimation for extremely large-scale MIMO: Far-field or near-field?" *IEEE Trans. Commun.*, vol. 70, no. 4, pp. 2663–2677, Apr. 2022.

[29] Y. Han, S. Jin, C. Wen, and X. Ma, "Channel estimation for extremely large-scale massive MIMO systems," *IEEE Wireless Commun. Lett.*, vol. 9, no. 5, pp. 633–637, May 2020.

[30] X. Zhang, H. Zhang, and Y. C. Eldar, "Near-field sparse channel representation and estimation in 6G wireless communications," *IEEE Trans. Commun.*, vol. 72, no. 1, pp. 450–464, Jan. 2024.

[31] J. Lee, G.-T. Gil, and Y. H. Lee, "Channel estimation via orthogonal matching pursuit for hybrid MIMO systems in millimeter wave communications," *IEEE Trans. Commun.*, vol. 64, no. 6, pp. 2370–2386, Jun. 2016.

[32] H. Lu and Y. Zeng, "Communicating with extremely large-scale array/surface: Unified modeling and performance analysis," *IEEE Trans. Wireless Commun.*, vol. 21, no. 6, pp. 4039–4053, Jun. 2022.

[33] C. A. Balanis, "Arrays: Linear, planar, and circular," in *Antenna Theory Analysis and Design*, 4th ed., Hoboken, NJ, USA: Wiley, 2016.

[34] R. He, B. Ai, G. Wang, M. Yang, C. Huang, and Z. Zhong, "Wireless channel sparsity: Measurement, analysis, and exploitation in estimation," *IEEE Wireless Commun.*, vol. 28, no. 4, pp. 113–119, Aug. 2021.

[35] C. Huang, L. Liu, C. Yuen, and S. Sun, "Iterative channel estimation using LSE and sparse message passing for mmWave MIMO systems," *IEEE Trans. Signal Process.*, vol. 67, no. 1, pp. 245–259, Jan. 2019.

[36] A. Pizzo, T. L. Marzetta, and L. Sanguinetti, "Degrees of freedom of holographic MIMO channels," in *Proc. IEEE 21st Int. Workshop Signal Process. Adv. Wireless Commun. (SPAWC)*, Atlanta, GA, USA, 2020, pp. 1–5.

[37] Y. C. Eldar, "Compressed sensing," in *Sampling Theory: Beyond Bandlimited Systems*, 1st ed., Cambridge, U.K.: Cambridge Univ. Press, 2015.

[38] J. Rodríguez-Fernández, N. González-Prelcic, K. Venugopal, and R. W. Heath, "Frequency-domain compressive channel estimation for frequency-selective hybrid millimeter wave MIMO systems," *IEEE Trans. Wireless Commun.*, vol. 17, no. 5, pp. 2946–2960, May 2018.

[39] *Spatial Channel Model for Multiple Input Multiple Output (MIMO) Simulations (Release 18)*, document TR 25.996, The 3rd Generation Partnership Project, Valbonne, France, Mar. 2024.
[40] *Study on Channel Model for Frequencies From 0.5 to 100 GHz (Release 18)*, document TR 38.901, The 3rd Generation Partnership Project, Valbonne, France, Mar. 2024.
[41] Z. Ben-Haim and Y. C. Eldar, "The Cramér-rao bound for estimating a sparse parameter vector," *IEEE Trans. Signal Process.*, vol. 58, no. 6, pp. 3384–3389, Jun. 2010.
[42] G. H. Golub and C. F. V. Loan, "Unsymmetric eigenvalue problems," in *Matrix Computations*, 4th ed., Baltimore, MD, USA: Johns Hopkins University Press, 2013.
[43] F. Gomez-Cuba and A. J. Goldsmith, "Sparse mmWave OFDM channel estimation using compressed sensing," in *Proc. IEEE Int. Conf. Commun. (ICC)*, Shanghai, China, May 2019, pp. 1–7.

Shaohua Yue (Graduate Student Member, IEEE) received the B.S. degree in electronic and information engineering from Peking University, China, in 2022, where he is currently pursuing the Ph.D. degree with the Department of Electronics. His current research interests include reconfigurable intelligent surfaces and holographic MIMO.

Shuhao Zeng (Member, IEEE) received the B.S. degree in communications engineering from Peking University in 2018 and the Ph.D. degree from the School of Electronics, Peking University, in 2023. He is currently a Post-Doctoral Researcher with Princeton University. His current research interests include reconfigurable intelligent surfaces enabled communication and sensing, and aerial access networks. He received the Best Doctoral Thesis Award from the Chinese Education Society of Electronics in 2023. He has served as the track chair and a TPC member for several IEEE conferences. He is currently an Editor of *Physical Communication*.

Liang Liu (Senior Member, IEEE) received the B.Eng. degree from Tianjin University, China, in 2010, and the Ph.D. degree from the National University of Singapore, Singapore, in 2014. From 2015 to 2017, he was a Post-Doctoral Fellow with the Department of Electrical and Computer Engineering, University of Toronto. From 2017 to 2018, he was a Research Fellow with the Department of Electrical and Computer Engineering, National University of Singapore. He is currently an Associate Professor with the Department of Electrical and Electronic Engineering, The Hong Kong Polytechnic University. He is the co-author of the book *Next Generation Multiple Access* (Wiley-IEEE Press). His research interests include next generation cellular technologies, such as machine-type communications for the Internet of Things and integrated sensing and communication. He was a recipient of the 2021 IEEE Signal Processing Society Best Paper Award, the 2017 IEEE Signal Processing Society Young Author Best Paper Award, the Best Student Award of 2022 IEEE International Conference on Acoustics, Speech, and Signal Processing (ICASSP), and the Best Paper Award of the 2011 International Conference on Wireless Communications and Signal Processing. He was recognized by the Clarivate Analytics as a Highly Cited Researcher in 2018. He was a Leading Guest Editor of IEEE WIRELESS COMMUNICATIONS Special Issue on Massive Machine-Type Communications for IoT. He is an Editor of IEEE TRANSACTIONS ON WIRELESS COMMUNICATIONS.

Yonina C. Eldar (Fellow, IEEE) received the B.Sc. degree in physics and the B.Sc. degree in electrical engineering from Tel Aviv University (TAU), Tel Aviv, Israel, in 1995 and 1996, respectively, and the Ph.D. degree in electrical engineering and computer science from Massachusetts Institute of Technology (MIT), Cambridge, MA, USA, in 2002.

She is currently a Professor with the Department of Mathematics and Computer Science, Weizmann Institute of Science, Rehovot, Israel, where she holds the Dorothy and Patrick Gorman Professorial Chair and heads the Center for Biomedical Engineering. Previously, she was a Professor with the Department of Electrical Engineering, Technion, where she held the Edwards Chair of Engineering. She is also a Visiting Professor with MIT, a Visiting Scientist with the Broad Institute, a Visiting Research Collaborator with Princeton University, an Adjunct Professor with Duke University, an Advisory Professor with Fudan University, a Distinguished Visiting Professor with Tsinghua University, and was a Visiting Professor with Stanford University. She is the author of the book *Sampling Theory: Beyond Bandlimited Systems* and the co-author of seven other books. Her research interests include statistical signal processing, sampling theory and compressed sensing, learning and optimization methods and their applications to biology, medical imaging, and optics.

Dr. Eldar is a member of the Israel Academy of Sciences and Humanities (elected 2017) and the Academia Europaea (elected 2023). She is also a fellow of EURASIP, the Asia–Pacific Artificial Intelligence Association, and the 8400 Health Network. She received many awards for excellence in research and teaching, including the IEEE Signal Processing Society Technical Achievement Award in 2013, the IEEE/AESS Fred Nathanson Memorial Radar Award in 2014, and the IEEE Kiyo Tomiyasu Award in 2016. She was a Horev Fellow of the Leaders in Science and Technology Program at the Technion and an Alon Fellow. She also received the Michael Bruno Memorial Award from the Rothschild Foundation, the Weizmann Prize for Exact Sciences, the Wolf Foundation Krill Prize for Excellence in Scientific Research, the Henry Taub Prize for Excellence in Research (twice), the Hershel Rich Innovation Award (three times), the Award for Women with Distinguished Contributions, the Andre and Bella Meyer Lectureship, the Career Development Chair at the Technion, the Muriel & David Jacknow Award for Excellence in Teaching, and the Technion's Award for Excellence in Teaching (two times). She received several best paper awards and best demo awards together with her research students and colleagues, including the SIAM Outstanding Paper Prize, the UFFC Outstanding Paper Award, the Signal Processing Society Best Paper Award, and the IET Circuits, Devices and Systems Premium Award. She was selected as one of the 50 most influential women in Israel and in Asia, and is a highly cited researcher. She was a member of the Young Israel Academy of Science and Humanities and the Israel Committee for Higher Education. She is the Editor-in-Chief of *Foundations and Trends in Signal Processing*, a member of the *IEEE Sensor Array and Multichannel Technical Committee*, and serves on several other IEEE committees. In the past, she was a Signal Processing Society Distinguished Lecturer, a member of the IEEE Signal Processing Theory and Methods and Bio Imaging Signal Processing technical committees, and served as an Associate Editor for IEEE TRANSACTIONS ON SIGNAL PROCESSING, the *EURASIP Journal of Signal Processing*, the *SIAM Journal on Matrix Analysis and Applications*, and the *SIAM Journal on Imaging Sciences*. She was the co-chair and the technical co-chair of several international conferences and workshops.

Boya Di (Member, IEEE) received the Ph.D. degree from the Department of Electronics, Peking University, China, in 2019. She was a Post-Doctoral Researcher with Imperial College London. Since 2021, she has been an Assistant Professor at Peking University. Her current research interests include holographic surfaces, AI-enabled communications, and aerial access networks. She was a recipient of the 2021 IEEE ComSoc Asia-Pacific Outstanding Paper Award, the 2022 IEEE ComSoc Asia-Pacific Outstanding Young Researcher Award, and the 2023 IEEE ComSoc TCCN Publication Award. She serves as an Associate Editor for IEEE TRANSACTIONS ON VEHICULAR TECHNOLOGY, IEEE COMMUNICATIONS SURVEYS AND TUTORIALS, and IEEE INTERNET OF THINGS JOURNAL.